

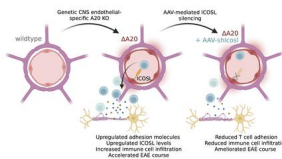
A20 regulates lymphocyte adhesion in murine neuroinflammation by restricting endothelial ICOSL expression in the CNS

Lisa Johann, ... , Markus Schwaninger, Ari Waisman

J Clin Invest. 2023. <https://doi.org/10.1172/JCI168314>.

Research In-Press Preview Autoimmunity Neuroscience

Graphical abstract



Find the latest version:

<https://jci.me/168314/pdf>



1 A20 regulates lymphocyte adhesion in murine neuroinflammation by restricting endothelial
2 ICOSL expression in the CNS

3

4 Lisa Johann¹, Sasha Soldati², Kristin Müller³, Josephine Lampe^{3,4}, Federico Marini^{5,6}, Matthias
5 Klein⁷, Eva Schramm¹, Nathalie Ries¹, Carsten Schelmbauer¹, Ilaria Palagi¹, Khalad Karram¹,
6 Julian C. Assmann³, Mahtab A. Khan³, Jan Wenzel^{3,4}, Mirko H. H. Schmidt⁸, Jakob Körbelin⁹,
7 Dirk Schlüter¹⁰, Geert van Loo^{11,12}, Tobias Bopp^{6,7}, Britta Engelhardt², Markus Schwaninger^{3,4}
8 and Ari Waisman^{1,6}

9

10 ¹ Institute for Molecular Medicine, University Medical Center of the Johannes Gutenberg
11 University Mainz, Mainz, Germany

12 ² Theodor Kocher Institute, University of Bern, Bern, Switzerland

13 ³ Institute for Experimental and Clinical Pharmacology and Toxicology, Center of Brain,
14 Behavior and Metabolism (CBBM), University of Lübeck, Lübeck, Germany

15 ⁴ DZHK (German Research Centre for Cardiovascular Research), Hamburg-Lübeck-Kiel,
16 Germany

17 ⁵ Institute of Medical Biostatistics, Epidemiology and Informatics (IMBEI), University Medical
18 Center of the Johannes Gutenberg University Mainz, Mainz, Germany

19 ⁶ Research Center for Immunotherapy (FZI), University Medical Center of the Johannes
20 Gutenberg University Mainz, Mainz, Germany

21 ⁷ Institute for Immunology, University Medical Center of the Johannes Gutenberg University
22 Mainz, Mainz, Germany

23 ⁸ Institute of Anatomy, Medical Faculty Carl Gustav Carus, Technische Universität Dresden
24 School of Medicine, Dresden, Germany

25 ⁹ University Medical Center Hamburg-Eppendorf, Department of Oncology, Hematology and
26 Bone Marrow Transplantation, Hamburg, Germany

27 ¹⁰ Hannover Medical School, Institute of Medical Microbiology and Hospital Epidemiology,
28 Hannover, Germany

29 ¹¹ Department of Biomedical Molecular Biology, Ghent University, Ghent, Belgium

30 ¹² VIB-UGent Center for Inflammation Research, Ghent, Belgium

31

32

33 Corresponding author:

34 Ari Waisman

35 Institute for Molecular Medicine, University Medical Center of the Johannes Gutenberg

36 University Mainz, Langenbeckstraße 1, 55131 Mainz, Germany

37 (+49) 6131-17-9129

38 waisman@uni-mainz.de

39

40 Conflict of interest:

41 JK is listed as inventor of a patent on AAV-BR1, held by Boehringer Ingelheim International

42 GmbH (patent no. US10696717B2). There are no other conflicts of interest to declare.

43

44 ABSTRACT

45 A20 is a ubiquitin-modifying protein that negatively regulates NF- κ B signaling. Mutations in
46 A20/*TNFAIP3* are associated with a variety of autoimmune diseases, including multiple
47 sclerosis (MS). We found that deletion of A20 in central nervous system (CNS) endothelial cells
48 (ECs) enhances experimental autoimmune encephalomyelitis (EAE), a mouse model of MS.
49 A20 ^{Δ CNS-EC} mice showed increased numbers of CNS-infiltrating immune cells during
50 neuroinflammation and in the steady state. While the integrity of the blood-brain barrier
51 (BBB) was not impaired, we observed a strong activation of CNS-ECs in these mice, with
52 dramatically increased levels of the adhesion molecules ICAM-1 and VCAM-1. We discovered
53 ICOSL as adhesion molecule expressed by A20-deficient CNS-ECs. Silencing of ICOSL in CNS
54 microvascular ECs partly reversed the phenotype of A20 ^{Δ CNS-EC} mice without reaching
55 statistical significance and delayed the onset of EAE symptoms in wildtype mice. In addition,
56 blocking of ICOSL on primary mouse brain microvascular endothelial cells (pMBMECs)
57 impaired the adhesion of T cells in vitro. Taken together, we here propose that CNS EC-ICOSL
58 contributes to the firm adhesion of T cells to the BBB, promoting their entry into the CNS and
59 eventually driving neuroinflammation.

60

64 INTRODUCTION

65 Multiple sclerosis (MS) is the most prevalent chronic inflammatory disease of the central
66 nervous system (CNS) in young adults (1). To date, the causes of MS are not fully understood,
67 yet it is presumed to be an autoimmune disease driven by autoreactive T cells targeting CNS
68 antigens (2). Upon reactivation at the CNS borders, autoreactive immune cells infiltrate the
69 CNS parenchyma and attack the myelin sheaths that surround neurons, eventually leading to
70 axonal loss and causing neuroinflammation (3,4).

71 Transmigration of T cells across the blood-brain barrier (BBB) represents a key step in the
72 pathology of MS and its animal model experimental autoimmune encephalomyelitis (EAE) (5),
73 which follows a multistep process involving interaction of different adhesion molecules with
74 integrins (6,7). While expression of these molecules on the BBB is usually low, pro-
75 inflammatory cytokine signaling during neuroinflammation induces dramatic brain
76 microvascular endothelial cell (BMEC) activation (8-12). IL-1 signaling is an essential pathway
77 driving the expression of adhesion molecules like intercellular adhesion molecule 1 (ICAM-1)
78 and vascular cell adhesion molecule 1 (VCAM-1) on BMECs through nuclear translocation of
79 nuclear factor 'kappa-light-chain-enhancer' of activated B cells (NF- κ B), thus promoting the
80 firm adhesion of leukocytes to the BBB (13-18).

81

82 A20 is an integral molecule for the negative regulation of the NF- κ B signaling pathway. The
83 transcription factor NF- κ B is active in BMECs in a variety of conditions associated with vascular
84 dysfunction and BBB impairment (19-21). Moreover, a protective role was ascribed to the NF-
85 κ B essential modulator (NEMO) and the upstream kinase TAK1 in BMECs, as their deletion
86 causes BBB disruption and BMEC cell death partly mediated by TNF signaling (22). Importantly,
87 A20 is well-known to counteract the cytotoxic effects of TNF (23-25).

88 Genetic variations in the *TNFAIP3* gene, encoding for A20, have been linked to the
89 susceptibility to MS (26). Interestingly, mice deficient for A20 develop a spontaneous
90 neuroinflammation with remarkable micro- and astrogliosis as well as BMEC activation (27).
91 Deletion of A20 specifically in astrocytes or microglia further proved the protective function
92 of A20 in the establishment of active EAE and spontaneous neuroinflammation (28-30).
93 Besides glial cells, also ECs express high levels of A20 in the steady state condition (31), yet
94 studies regarding the role of A20 in CNS-ECs are so far lacking.

95

96 We found that mice lacking A20 in CNS-ECs develop an exacerbated EAE disease upon
97 adoptive transfer (AT) of encephalitogenic T cells. While we did not observe pronounced
98 alterations in the structure of the microvasculature or BBB integrity, we found that loss of A20
99 in CNS-ECs dramatically upregulates ICAM-1, VCAM-1 and the Inducible T cell co-stimulator
100 ligand (ICOSL). Using a CNS-microvasculature endothelial cell-specific viral vector to silence
101 ICOSL, we could partly rescue the more severe AT-EAE course in A20^{ΔCNS-EC} mice and delay the
102 onset of an active EAE disease in wildtype mice. Mechanistically, we demonstrate that ICOSL
103 drives the adhesion of Th1 and Th17 cells to an in vitro BBB model. Taken together, our work
104 reveals A20-regulated ICOSL as an adhesion molecule involved in the multi-step
105 transmigration process of T cells across the BBB under inflammatory conditions.

106

107 RESULTS

108 *Mice with A20-deficient CNS-ECs are hypersensitive to adoptive transfer experimental*
109 *autoimmune encephalomyelitis*

110 To investigate the involvement of CNS-endothelial A20 in autoimmune neuroinflammation we
111 generated A20^{ΔCNS-EC} mice which lack A20 in CNS-ECs upon tamoxifen (TAM)-inducible Cre

112 recombination (Figure 1A). RT-PCR and Western blot analyses of primary mouse brain
113 microvascular endothelial cells (pMBMECs) confirmed the deletion of *Tnfrsf3/A20* (Figure 1B,
114 C). To our surprise, we did not observe a difference in disease severity between $A20^{\Delta\text{CNS-EC}}$
115 mice and littermate controls in three different active EAE models where mice were immunized
116 with MOG₃₅₋₅₅ in complete Freund's adjuvant (CFA) (Supplemental Figure 1A-L). As CFA is
117 known to activate CNS-ECs (13), we next studied the phenotype of $A20^{\Delta\text{CNS-EC}}$ mice in an
118 adoptive transfer (AT)-EAE model which circumvents CFA-driven effects.

119 Interestingly, we found that compared to littermate controls, the majority of $A20^{\Delta\text{CNS-EC}}$ mice
120 developed EAE symptoms (Figure 1D). This resulted in an increased average disease severity,
121 with increased area under the curve (AUC) values and maximum scores (Figure 1E-G). $A20^{\Delta\text{CNS-}}$
122 $^{\text{EC}}$ mice furthermore showed a tendency towards earlier disease onset (Figure 1H). To exclude
123 astrocytic contamination as previously reported for the *Slco1c1-CreER^{T2}* mouse line (32) we
124 generated mice lacking A20 in all endothelial cells ($A20^{\Delta\text{EC}}$) by crossing $A20^{\text{fl/fl}}$ mice to
125 *Cdh5(PAC)-CreER^{T2}* mice (33) to validate our data. Indeed, we observed a very similar
126 phenotype with an overall increased disease severity (Figure 1I-K). $A20^{\Delta\text{EC}}$ mice furthermore
127 showed a significantly accelerated disease onset, with mice developing symptoms in average
128 two days earlier than controls (Figure 1L).

129 We next focused on a different model involving CNS inflammation and used an MCAO model
130 to induce stroke in $A20^{\Delta\text{CNS-EC}}$ mice. We observed significantly increased infarct and edema
131 volumes, overall leading to a mildly increased edema-corrected infarct volume in $A20^{\Delta\text{CNS-EC}}$
132 mice (Supplemental Figure 2). Together, this data strongly suggests a protective role for CNS
133 EC-A20 in CNS autoimmunity and sterile inflammation.

134

135 *Loss of A20 in CNS-ECs drives immune cell infiltration into the CNS*

136 To investigate the extent of leukocyte infiltration, we isolated immune cells from the SC at the
137 peak of AT-EAE disease and analyzed cell subsets and cytokine production by flow cytometry
138 after antigen recall (Figure 2A). We found dramatically increased numbers of CD45.1⁺
139 transferred and amongst them CD40L⁺ MOG₃₅₋₅₅-specific T cells in A20^{ΔCNS-EC} mice (Figure 2B,
140 C). Also, the number of cytokine-producing cells was significantly increased (Figure 2D-F).
141 Furthermore, absolute cell counts of dendritic cells, neutrophils and monocytes were elevated
142 in A20^{ΔCNS-EC} mice (Supplemental Figure 3A-E). We next analyzed the location of CD3⁺ T cells
143 in the SC by immunostaining. Compared to controls, we found high numbers of T cells in the
144 SC of A20^{ΔCNS-EC} mice, with cells forming perivascular cuffs but also penetrating deep into the
145 parenchyma (Figure 2G). As EAE disease severity is strongly dependent on the ratio of effector
146 to regulatory T cells (Treg cells) (34), we next assessed if loss of A20 in CNS-ECs influences Treg
147 cell frequencies. We did not observe changes in Treg cell frequencies or effector T cell to Treg
148 cell ratio at day post transfer (DPT) 18 (Supplemental Figure 4A-D). Based on these
149 observations, we conclude that the loss of A20 in CNS-ECs promotes immune cell infiltration
150 across the BBB under inflammatory conditions without affecting the proportion of effector T
151 cells to Treg cells.

152 We next addressed the question whether loss of A20 in CNS-ECs causes infiltration of immune
153 cells even in the absence of exogenously induced inflammation. We assessed the numbers of
154 CD45⁺ total infiltrates, TCRβ⁺ T cells and CD11b⁺ myeloid cells in the steady state CNS one
155 week after TAM injection. Indeed, we found increased numbers of immune cells infiltrating
156 the CNS in A20^{ΔCNS-EC} mice in the steady state compared to littermate controls (Figure 2H-J,
157 Supplemental Figure 3F, G). Interestingly, the frequencies of TCRβ⁺ T cells and CD11b⁺ myeloid
158 cells amongst all infiltrating cells were not altered (Supplemental Figure 3H). Taken together,

159 this data suggests that the loss of A20 in CNS-ECs provokes the infiltration of immune cells
160 across the BBB even in the absence of an inflammatory stimulus.

161

162 *A20 protects from excessive adhesion molecule expression in steady state CNS-ECs*

163 To test whether deficiency for A20 in BMECs results in CNS blood vessel abnormalities, we
164 performed immunostainings of the endothelial cell marker CD31 and of collagen IV as an
165 integral basement membrane component. We neither observed alterations in vessel length
166 nor increased numbers of empty basement membrane strands, also known as string vessels
167 (35), in the brains of A20^{ΔCNS-EC} mice (Figure 3A, B). We next focused on BBB integrity in
168 A20^{ΔCNS-EC} mice. By performing immunostaining for the tight junction molecule occludin, we
169 observed reduced fluorescence intensity in BMECs of A20^{ΔCNS-EC} mice (Figure 3E, F). However,
170 brain weight, as an indicator of brain edema, was not increased compared to controls (Figure
171 3D). To exclude a disruption of the BBB and the blood-spinal cord barrier (BSCB), we assessed
172 the integrity by injecting a small 3-5 kDa dextran tracer and measuring fluorescence in brain
173 or SC. Compared to mice at the peak of an active EAE disease, in which BBB and BSCB integrity
174 are compromised, A20^{ΔCNS-EC} mice did not show an increased permeability for FITC-dextran,
175 confirming normal BBB and BSCB integrities (Figure 3G, H).

176 As T cell transmigration across the BBB is mainly dependent on the surface expression levels
177 of adhesion molecules (36), we next investigated if the increased numbers of immune cells
178 infiltrating the CNS in A20^{ΔCNS-EC} mice were due to alterations in adhesion molecule expression.
179 By performing immunostaining of VCAM-1 together with collagen IV, we detected
180 dramatically increased numbers of VCAM-1⁺ microvessels in the brain cortex of A20^{ΔCNS-EC} mice
181 (Figure 4A, B). Also, ICAM-1 levels were dramatically increased on CNS microvessels in A20^{ΔCNS-}
182 ^{EC} mice, with almost 100% of CNS-ECs expressing ICAM-1 (Figure 4C-F). Both molecules are

183 well-known to mediate the multistep process of immune cell transmigration across the BBB
184 (6). Our data suggests that loss of A20 in CNS-ECs does not influence BBB integrity but causes
185 a dramatic upregulation of cell adhesion molecules, which at least partially drives leukocyte
186 infiltration and AT-EAE severity.

187

188 *RNA-seq reveals strong activation of CNS-ECs in A20^{ΔCNS-EC} mice*

189 Blocking immune cell infiltration by targeting α 4-integrin, a binding partner of VCAM-1, with
190 natalizumab is an effective treatment option for MS patients presenting with a relapsing-
191 remitting disease course (37-39). Yet, this therapeutic strategy comes with a risk to develop
192 severe CNS infections (40). Identification of novel adhesion molecules facilitating the
193 extravasation of specific cell subsets is thus essential. We therefore made use of the A20<sup>ΔCNS-
194 EC</sup> mice to characterize their CNS-EC adhesion molecule profile in-depth by RNA sequencing.
195 Crossing these mice to R26R-EYFP reporter mice allowed us to sort for CNS-ECs from the SC
196 with Cre-mediated recombination, which could be observed in approximately 90% of all ECs
197 (Supplemental Figure 5A, B). To focus on molecules involved in immune cell transmigration,
198 we included a control group of wildtype-like A20^{fl/fl} mice at day post immunization (DPI) 10 of
199 an active EAE disease, a timepoint where immune cell extravasation across the BBB is known
200 to happen (41). We first confirmed the purity of the sorted SC-ECs by plotting endothelial
201 marker genes as well as genes specific for other CNS-resident cells (Figure 5A). We next
202 focused on genes that were differentially expressed (DE) in either the A20^{ΔCNS-EC}-eYFP or the
203 EAE group compared to the control condition, respectively. While most of the DE genes were
204 found in the EAE situation, a substantial amount of DE genes could also be identified in
205 A20^{ΔCNS-EC}-eYFP mice (Figure 5B). The overlap of DE genes in the A20^{ΔCNS-EC}-eYFP and the EAE
206 condition resulted in 26 genes that were commonly upregulated and 4 genes that were

207 commonly downregulated (Figure 5C, D). Amongst these genes, *Icam1* and *Vcam1*
208 represented the top upregulated genes, confirming our previous findings. Also, *Tnfaip3* itself
209 was among the upregulated genes, yet mapping the reads of *Tnfaip3* to the genetic locus
210 confirmed the excision of exon 3 in A20^{ΔCNS-EC} mice, rendering the transcript non-translatable
211 (Supplemental Figure 5C) (42). To investigate if other genes related to immune cell
212 transmigration across the BBB were amongst the commonly DE genes, we performed a KEGG
213 pathway analysis. The most prominent pathways were the inflammatory *NF-κB* and *TNF*
214 *signaling pathways*, pointing out the essential function of A20 as negative regulator of these
215 signaling cascades. Interestingly, and as hypothesized, also the *Cell adhesion molecules*
216 pathway was amongst the top KEGG terms (Figure 5E). This was further underscored by a
217 Gene Ontology (GO) term analysis, in which *Leukocyte cell-cell adhesion*, *Membrane to*
218 *membrane docking* and *Cell adhesion* represented the top affected Biological Processes
219 (Suppl. Figure 5D).

220

221 *ICOSL is upregulated on CNS-ECs under inflammatory conditions*

222 Interestingly, besides *Icam1* and *Vcam1* also *Icosl* was identified as cell adhesion molecule in
223 the KEGG pathway analysis and moreover, *Icosl* expression levels in A20^{ΔCNS-ECs} and DPI10 ECs
224 were very similar to those of *Icam1* and *Vcam1* (Supplemental Figure 5E). RT-PCR validation
225 of *Icosl* expression indeed confirmed its upregulation in sorted CNS-ECs from naïve A20^{ΔCNS-EC}
226 mice compared to littermate controls (Supplemental Figure 5F). In addition, we could validate
227 the upregulation of ICOSL protein on CNS-ECs in vivo during EAE (Figure 5F, G).

228

229 Expression of ICOSL on peripheral ECs as well as on the human BMEC-derived cell line
230 hCMEC/D3 is strongly upregulated by various inflammatory stimuli in vitro (43,44). We thus

231 investigated *Icosl* mRNA levels in pMBMECs isolated from A20^{ΔCNS-EC} mice and found increased
232 levels in response to TNF stimulation compared to unstimulated or TNF-stimulated A20^{fl/fl}
233 control pMBMECs (Supplemental Figure 5G). Furthermore, while TNF stimulation of wildtype
234 pMBMECs significantly increases *Icosl* expression, IL-1β stimulation led to an even higher
235 upregulation of *Icosl* mRNA levels (Supplemental Figure 5H). Moreover, ICOSL upregulation in
236 response to IL-1β stimulation followed a very similar pattern like ICAM-1 and VCAM-1
237 (Supplemental Figure 5I). These data indicate that in addition to ICAM-1 and VCAM-1, also
238 ICOSL is upregulated on CNS-ECs under inflammatory conditions and may therefore contribute
239 to the onset of neuroinflammation.

240

241 *Silencing of CNS microvascular EC-ICOSL ameliorates AT-EAE in A20^{ΔCNS-EC} mice*

242 To evaluate the function of CNS EC-ICOSL in autoimmune neuroinflammation, we knocked
243 down ICOSL by delivering shRNA to CNS microvascular ECs using the AAV-BR1. As not 100% of
244 CNS microvascular ECs are transduced upon AAV-BR1 application (45), we first confirmed that
245 the location of the transduced ECs was in close proximity to the infiltrating immune cells
246 during EAE. Indeed, we found multiple GFP⁺ vessels in close proximity to CD3⁺ T cells in the
247 perivascular space, but also in close proximity to T cells infiltrating into the SC parenchyma in
248 EAE mice treated with AAV-BR1-eGFP (Figure 6A, B). Immunofluorescence furthermore
249 proved specificity of the AAV-BR1-eGFP in targeting vessels, as eGFP only co-localized with
250 laminin but not cortical neuronal NeuN (Supplemental Figure 6A). Next, we designed a CNS
251 microvascular EC-specific AAV carrying either an shRNA against *Icosl* (AAV-BR1-shIcosl) or a
252 scrambled shRNA (AAV-BR1-con) (Figure 6C). Both constructs express a GFP reporter under
253 the relatively weak RSV promoter, which was chosen to exclude potential GFP-induced
254 cytotoxicity (46). Yet, GFP intensity was still strong enough to validate the target specificity.

255 Upon injection of the AAV-BR1-shIcosl construct, GFP⁺ cells could only be found among the
256 CD31⁺ Ly6C⁺ EC population, but not in other CNS-resident cells (Supplemental Figure 6B-F).
257 Transduction of pMBMECs with AAV-BR1-shIcosl furthermore proved the efficiency of this
258 virus to knockdown *Icosl* as expression levels were reduced by approximately 70% in IL-1 β
259 stimulated pMBMECs (Supplemental Fig 6G). Flow cytometry of CNS-ECs upon in vivo
260 administration of AAV-BR1-shIcosl furthermore demonstrated a significant reduction in the
261 mean fluorescence intensity of ICOSL as well as in the percentage of ICOSL⁺ ECs in mice after
262 immunization with MOG₃₅₋₅₅/CFA (Figure 6D, E). Of note, treatment with AAV-BR1-shIcosl did
263 not influence protein levels of ICAM-1 or VCAM-1 in CNS-ECs (Supplemental Figure 6H, I).

264

265 We next used this system to knockdown ICOSL in CNS microvascular ECs in A20^{ΔCNS-EC} mice to
266 evaluate the contribution of ICOSL to their increased EAE phenotype. Administration of AAV-
267 BR1-shIcosl, but not AAV-BR1-con, mildly ameliorated the AT-EAE disease course including the
268 area under the curve, the day of onset and the score at DPT7, a timepoint shortly after disease
269 onset (Figure 6F-I). Furthermore, AAV-BR1-shIcosl administration significantly reduced the
270 number of transferred CD45.1⁺ T cells infiltrating into the SC (Figure 6J). Thus, ICOSL
271 participates in driving autoimmune neuroinflammation in A20^{ΔCNS-EC} mice and its knockdown
272 reduces the infiltration of encephalitogenic cells into the CNS.

273

274 *Endothelial ICOSL influences day of active EAE onset in wildtype mice*

275 Next, we wanted to recapitulate our findings in wildtype mice in an active EAE model. For this,
276 AAV-BR1-shIcosl was injected i.v. and two weeks later mice were immunized with MOG₃₅₋₅₅ in
277 CFA. Confirming our previous findings, we also detected a mildly ameliorated disease and a
278 tendency towards reduced numbers of infiltrating immune cells in mice treated with AAV-

279 BR1-shIcosl (Figure 6K-O). More importantly, disease onset could be delayed by an average of
280 two days in the AAV-BR1-shIcosl treated group (Figure 6M). These findings confirm a
281 functional role for CNS microvascular EC-ICOSL in driving autoimmune neuroinflammation,
282 possibly by promoting the infiltration of pathogenic T cells.

283

284 *ICOSL promotes T-cell adhesion to the BBB in vitro*

285 ICOSL is an immunoglobulin superfamily member, expressing immunoglobulin-like domains
286 that are known to mediate cell-cell adhesion through binding in a homophilic or heterophilic
287 manner (47). ICOSL thus shares structural similarities with the known adhesion molecules
288 ICAM-1, VCAM-1 and the more recently characterized molecules activated leukocyte adhesion
289 molecule (ALCAM-1), melanoma cell adhesion molecule (MCAM-1) and dual immunoglobulin-
290 domain containing cell adhesion molecule (DICAM-1) (48-52). Recently, it was shown that
291 ICOSL can bind to $\alpha_v\beta_3$, an integrin known to be important for EAE development by mediating
292 the recruitment of encephalitogenic T cells to the CNS (53,54). This body of evidence led us to
293 hypothesize that CNS EC-ICOSL could be involved in mediating immune cell adhesion to the
294 BBB. To prove this, we performed T cell migration assays as well as static T cell adhesion assays
295 on anti-ICOSL-treated pMBMECs. We found significantly reduced numbers of adhering MOG₃₅₋
296 ₅₅-specific Th1 and Th17 cells under static conditions when ICOSL was blocked on IL-1 β -
297 stimulated pMBMECs (Figure 7A-C). We next assessed the post-arrest behavior of Th1 cells
298 under physiological flow conditions. The numbers of arrested T cells showed a trend towards
299 lower numbers of cells arresting when ICOSL was blocked, however, due to the variance across
300 the individual experiments not reaching statistical significance (Figure 7D). The post-arrest
301 behavior, which we categorized into fractions of T cells that were detaching, probing, probing
302 followed by diapedesis, crawling and crawling followed by diapedesis, was unaltered when

303 ICOSL was blocked (Figure 7E). Also, the crawling distance and crawling speed of the T cells
304 that successfully performed diapedesis following crawling on the pMBMECs was not changed
305 (Figure 7F, G). Taken together, ICOSL promotes the arrest of Th1 and Th17 cells to the
306 monolayer without influencing the post-arrest behavior of T cells on pMBMECs under
307 physiological flow.

308

309 DISCUSSION

310 In this study, we identified a previously unknown role of CNS-EC A20 in neuroinflammation.
311 Our results show that the loss of A20 in CNS-ECs strongly increased the risk to develop EAE
312 upon transfer of encephalitogenic T cells into naïve recipients and accelerates disease onset.
313 ECs lacking A20 were dramatically activated which resulted in the upregulation of cell
314 adhesion molecules like ICAM-1 and VCAM-1 but also ICOSL. We propose here that A20 serves
315 as a gatekeeper for the activation of ECs, and its absence drives transmigration of
316 encephalitogenic T cells across the BBB and by this, at least partially, contributes to the
317 increased disease susceptibility.

318 Supporting evidence for this hypothesis comes from the observation that innate immune
319 activation, for example mediated by CFA used in the active EAE induction protocol, drives
320 endothelial activation and promotes upregulation of adhesion molecules already before onset
321 of disease, suggesting a causal role for endothelial activation in disease initiation (13,55,56).
322 Interestingly, and in contrast to A20-deficiency in microglia and astrocytes (28,29), we did not
323 observe alterations in an actively induced EAE disease in mice with A20-deficient ECs. It seems
324 likely that the endothelial activation in response to CFA in the active EAE model masks the
325 effects driven by A20 deletion in CNS-ECs and could thus explain the difference seen in AT-
326 EAE but not active EAE outcomes.

327

328 We observed an increased infiltration of immune cells into the CNS of A20^{ΔCNS-EC} mice in steady
329 state and after AT-EAE. To enter the CNS, immune cells need to cross the BBB, which
330 represents a key step in the pathology of CNS autoimmune diseases such as MS. Both immune
331 cells and BMECs require a certain state of activation to allow immune cells to cross the BBB.
332 The influence of cytokines and other inflammatory mediators secreted by activated T cells but
333 also innate immune cells on the endothelium has been extensively described (57-59). In
334 particular, pro-inflammatory cytokines like TNF or IL-1 β that activate the NF- κ B pathway are
335 essential in mediating the upregulation of cell adhesion molecules on BMECs which promote
336 the infiltration of pathogenic T cells and the development of CNS autoimmunity (13,60,61).
337 Upregulation of ICAM-1 and VCAM-1 in CNS-ECs has been described in A20^{-/-} mice in the
338 steady-state, however, it was suggested that this upregulation of adhesion molecules was due
339 to the overall heightened cerebral inflammation present in A20^{-/-} mice (27). Opposingly, we
340 show here that ICAM-1 and VCAM-1 upregulation in steady-state CNS-ECs was driven by an
341 endothelial-intrinsic response to A20-deficiency, as A20^{ΔCNS-EC} mice manifested a strong
342 expression of both molecules without external inflammatory stimulation.

343 Our results furthermore indicate that rather excessive adhesion molecule expression and not
344 BBB breakdown are responsible for the pronounced CNS immune cell infiltration in A20^{ΔCNS-EC}
345 mice. It was earlier proposed that NF- κ B signaling in BMECs is essential for maintaining barrier
346 integrity (22). Disruption of NF- κ B signaling through CNS EC-specific deletion of NEMO or TAK1
347 resulted in an increased BBB permeability which was suggested to result from impaired A20-
348 mediated occludin stabilization (22). Although we could confirm that A20-deficiency in CNS-
349 ECs leads to decreased occludin levels, this reduction did not cause BBB or BSCB breakdown
350 in our study, underscoring the debate about the necessity of occludin for barrier integrity (62-

351 65). Our data furthermore corroborates earlier reports of A20^{-/-} and A20^{+/-} mice, which also
352 did not manifest any signs of BBB disruption (27,66). We can thus conclude that activation of
353 BMECs through loss of A20 provokes expression of cell adhesion molecules which promotes
354 the firm adhesion of immune cells to the BBB and facilitates their entry into the CNS.
355 Supporting our findings, we furthermore found a more severe disease pathology in the MCAO
356 model, a model involving sterile CNS inflammation, in A20^{ΔCNS-EC} mice. Interestingly, T cells
357 infiltrate into the injured areas as early as 24h post MCAO induction (67) and blocking of the
358 α4-integrin unit of VLA-4, the binding partner of VCAM-1, reduces the infarct volumes by
359 restricting CNS T cell infiltration (68,69). It is thus possible, that the increased infarct areas in
360 A20^{ΔCNS-EC} arise from a more pronounced T cell infiltration due to the massive EC activation.

361

362 The success of targeting the VLA-4 subunit α4-integrin with natalizumab in MS therapy points
363 out the attractiveness of interfering with transmigration of immune cells across the BBB in
364 diseases involving CNS inflammation. Yet, due to the potential side effects of this treatment
365 strategy it is necessary to identify alternative targets for therapeutic intervention. In recent
366 years, alternative cell adhesion molecules involved in immune cell transmigration across the
367 BBB have been identified. ALCAM was found to be an important adhesion molecule guiding B
368 cell and monocyte trafficking across the BBB, yet deletion of this molecule dramatically
369 influences the barrier integrity and causes more severe EAE disease (48,49,70). Also, MCAM
370 was implicated in several studies to be essential for CD8⁺ as well as Th17 cell migration across
371 the BBB (50,51,71). More recently, also DICAM was found to be involved in Th17 cell migration
372 across the BBB and was suggested as a potential target in progressive MS forms (52). While
373 progress has been made in recent years, the spectrum of molecular interactions occurring at
374 the CNS-peripheral interface is certainly not yet disentangled in its entirety. We here identified

375 A20-regulated ICOSL as adhesion molecule contributing to the firm adhesion of MOG₃₅₋₅₅
376 specific pro-inflammatory Th1 and Th17 cells to the BBB. Although the reduction in T cell
377 adhesion when ICOSL was blocked appears rather mild, the effect is in line with studies
378 investigating T cell adhesion to other adhesion molecules (52,72). ICOSL was only recently
379 reported to mediate adhesion of podocytes by binding to the $\alpha_v\beta_3$ integrin through its RGD
380 motif (54). Interestingly, Roussel *et al.* earlier introduced a human mutation in ICOSL, which
381 was found in one patient with a combined immunodeficiency syndrome (73). The authors
382 identified an involvement of endothelial ICOSL in mediating the transmigration of T cells and
383 neutrophils across an in vitro endothelial barrier (73). We here corroborate these findings and
384 extent the involvement of endothelial ICOSL in immune cell adhesion from the periphery to
385 brain-derived pMBMECs. Future studies are, however, necessary to determine the exact
386 binding partner of ICOSL that mediates this adhesion and to further characterize the spectrum
387 of immune cells having the capacity to bind to ICOSL.

388

389 We could furthermore underscore the functional role of CNS EC-ICOSL in the development of
390 autoimmune neuroinflammation by in vivo silencing of ICOSL with a CNS-microvascular
391 endothelial specific AAV. Although the GFP signal from our AAV-BR1-shIcosl likely
392 underrepresents the percentage of transduced cells due to the comparably weak RSV
393 promoter driving GFP expression, we could confirm the efficiency of our construct to knock
394 down ICOSL specifically in CNS-ECs both in vitro and in vivo. More importantly, we were able
395 to partly rescue the accelerated disease outcome in A20^{ACNS-EC} mice by treating them with
396 AAV-BR1-shIcosl, although not reaching statistical significance. Notably, and opposed to
397 observations from Roussel *et al.*, protein levels of ICAM-1 and VCAM-1 molecules were not
398 affected by silencing of ICOSL (73). The high levels of these molecules remaining in A20^{ACNS-EC}

399 mice might explain the rather mild amelioration in the day of disease onset and the overall
400 disease severity upon treatment with AAV-BR1-shIcosl. Nevertheless, silencing of ICOSL on
401 CNS-ECs restricted the infiltration of transferred encephalitogenic T cells into the CNS of
402 A20^{ΔCNS-EC} mice, confirming its contribution to T-cell mediated autoimmunity.

403

404 In agreement with these observations, our results additionally showed that the day of active
405 EAE onset could be delayed when ICOSL was knocked down in CNS-ECs of wildtype mice. As
406 transmigration of immune cells through the BBB precedes the development of EAE symptoms
407 (74,75), our data suggests that the delayed disease development is due to an impairment of T
408 cell adhesion to the BBB. The phenotype we observed is in accordance with EAE data from
409 mice in which other cell adhesion molecules (ICAM-1, ICAM-2, VCAM-1) were targeted
410 (36,76). Targeting of CNS microvascular EC-ICOSL thus seems to be an attractive approach for
411 controlling infiltration of pathogenic immune cells in the context of autoimmune
412 neuroinflammation. However, ICOSL is well-known to also function as co-stimulatory
413 molecule in an immunological context (77-79) and earlier studies targeting ICOS indicated a
414 protective effect of ICOS-ICOSL interaction in the priming phase of EAE (80,81). Thus, anti-
415 ICOSL treatment for CNS autoimmunity needs to be carefully evaluated as the desired effect
416 strongly relies on cell specificity as well as the time point of therapy.

417

418 In conclusion, our study sheds new light on two important aspects in the pathology of CNS
419 inflammation. Firstly, our data demonstrates a protective role for CNS endothelial A20 by
420 preventing the excessive expression of cell adhesion molecules and thus regulating the
421 infiltration of immune cells into the CNS. Secondly, we discovered ICOSL as an A20-regulated
422 cell adhesion molecule mediating the firm adhesion of Th1 and Th17 cells to the BBB. Overall,

423 this study suggests ICOSL as a potential therapeutic target in the treatment of CNS
424 autoimmune diseases such as MS.

425 426 METHODS

427 *Mice*

428 All mice used were on the C57BL/6 background and housed under specific pathogen-free
429 conditions. A20^{fl/fl} mice (82) were crossed to Slco1c1-CreER^{T2} mice (32) (A20^{ACNS-EC}) and used
430 for A20 western blot analysis, immunofluorescent stainings of brain vessels with collagen IV,
431 CD31, occludin and VCAM-1, MCAO and active EAE in facility 2. For all other experiments
432 analyzing A20^{ACNS-EC} mice, A20^{fl/fl} mice (42) were crossed to Slco1c1-CreER^{T2} mice (32). For
433 generation of A20^{ΔEC} mice, A20^{fl/fl} mice (42) were crossed to Cdh5(PAC)-CreER^{T2} (33) mice. Cre-
434 negative A20^{fl/fl} littermates were used as controls. For sequencing experiments, A20^{ACNS-EC}
435 mice were crossed to R26R-EYFP reporter mice (83). For AT-EAE experiments, Ly5.1 mice
436 (B6.SJL-PtprcaPepcb/BoyCrI) were used as donor mice.

437

438 *Tamoxifen treatment*

439 A 20 mg/ml tamoxifen (Sigma-Aldrich) solution was prepared by suspension in olive oil (Sigma-
440 Aldrich) containing 5 % ethanol. Tamoxifen was dissolved by rotation overnight at 4°C. Mice
441 were injected intraperitoneally (i.p.) with 100 μl (= 2 mg tamoxifen) at five (for Slco1c1-CreER^{T2}
442 strains) or three (for Cdh5(PAC)-CreER^{T2} strains) consecutive days at the age of 6-7 weeks and
443 mice were used for experiments 2-4 weeks thereafter, unless otherwise indicated. A20^{fl/fl}
444 littermate controls were treated equally.

445

446 *Active EAE induction*

447 An emulsion of MOG₃₅₋₅₅ in CFA was prepared by mixing 1 mg/ml MOG₃₅₋₅₅ (GenScript) in PBS
448 with Complete Freund's Adjuvants (CFA, BD Biosciences) supplemented with *Mycobacterium*
449 *tuberculosis* H37RA (BD Biosciences). 50 µg MOG₃₅₋₅₅/CFA were injected subcutaneously into
450 the tail base. At the day of immunization and two days later, 150 ng pertussis toxin (PTx, List
451 Biological Laboratories) in PBS were applied i.p. unless otherwise stated. For active EAE
452 induction in facility 2 (Supplemental Figure 1E-H) mice were immunized with an immunizing
453 emulsion (EK-2110, Hooke Laboratories) containing a MOG₃₅₋₅₅ peptide in Freund's adjuvant
454 as described before (84). Additionally, mice were treated with 400 ng PTx i.p. on the day of
455 immunization and one day later.

456 Mice were weighed daily and clinical scores were documented as follows: 0, no disease; 0.5:
457 limb tail; 1: paralyzed tail; 1.5: weakened righting reflex; 2: no righting reflex; 3: partial
458 paralysis of hind legs; 3.5: paralysis of one hind leg; 4: paralysis of both hind legs.

459

460 *Adoptive transfer (AT) EAE induction*

461 Ly5.1 mice were immunized with MOG/CFA and PTx as described above. Ten days after
462 immunization, spleen, inguinal and paraaortic lymph nodes were harvested and single-cell
463 suspensions were prepared and cultured in vitro in the presence of MOG₃₅₋₅₅ peptide (20
464 µg/ml), anti-IFNγ (10 µg/ml; BioXCell), and IL-23 (15 ng/ml; Miltenyi Biotec). After 4 days, cells
465 were harvested and examined for blasting lymphocytes, as based on forward and side scatter
466 properties in flow cytometry. Cell suspensions were adjusted to 50 × 10⁶ blasting cells/ml, and
467 100 µl of this suspension was injected intravenously (i.v.) into the tail veins of recipient mice,
468 accompanied by i.p. injections of PTx (150 ng) at the same day and 2 days later. Mice were
469 weighed daily and the clinical scores were assessed according to the scoring system described
470 above.

471

472 *Permanent occlusion of the middle cerebral artery (MCAO)*

473 The ischemic stroke model was performed as described before (85). Briefly, mice were
474 anaesthetized using tribromoethanol (2.5%, 15 μ l/g body weight, i.p.). After a skin incision and
475 removal of the left temporal muscle, a burr hole was drilled through which the stem of the
476 middle cerebral artery was occluded by electrocoagulation (Model ICC50, Erbe). After
477 suturing, mice were placed under a heating lamp until they fully recovered. After 48h, mice
478 were perfused intracardially under deep anesthesia and brains were removed. Coronal
479 cryosections were cut every 400 μ m and stained using a silver technique (86). Infarcted areas
480 were measured using ImageJ and infarct volume, edema, and edema-corrected infarct volume
481 were calculated as described before (86).

482

483 *Immunofluorescence staining*

484 Immunofluorescence stainings were performed on fixed frozen sections of 10-20 μ m. Primary
485 antibodies against CD3 ϵ (145-2C11, Armenian hamster monoclonal, eBioscienceTM, Thermo
486 Fisher Scientific, 1:100), NeuN (1B7, Mouse monoclonal, Invitrogen Thermo Fisher Scientific,
487 1:500), CD31 (rabbit polyclonal, abcam, 1:100 or MEC 13.3, rat monoclonal, BD PharmingenTM,
488 1:500), laminin 1+2 (rabbit polyclonal, abcam, 1:500), collagen IV (rabbit polyclonal, abcam,
489 1:1000), occludin (rabbit polyclonal, Proteintech, 1:1000) and VCAM-1 (MVCAM.A, rat
490 monoclonal, BD PharmingenTM, 1:1000) were incubated over night at 4°C. Sections were
491 washed and secondary antibodies against rabbit IgG (CF488A, Sigma-Aldrich, 1:800 or CFTM
492 555, Sigma-Aldrich, 1:800 or Cy3, Jackson ImmunoResearch Labs, 1:400), Armenian hamster
493 (Alexa Fluor 647, Jackson ImmunoResearch Labs, 1:800), mouse IgG (CFTM 647, Sigma-Aldrich,
494 1:500) or rat IgG (Alexa 488, Thermo Fisher Scientific, 1:400) were added for 45 min - 1.5 h at

495 room temperature. Afterwards, sections were mounted with DAPI Fluoromount-G® Mounting
496 Medium (SouthernBiotech) or Mowiol 4-88 (Carl Roth) and images were acquired at a TCS SP8
497 inverse confocal microscope (Leica) or a DMI 6000B fluorescence microscope (Leica). Images
498 were analyzed with ImageJ software as described before (22).

499

500 *Culture of primary murine brain microvascular endothelial cells (pMBMEC)*

501 Cortices from 8-12-week-old wildtype mice were used for pMBMEC isolation as described
502 previously (87). Cells were seeded on 48-well culture dishes coated with Matrigel (ECM Gel
503 from Engelbreth-Holm-Swarm murine sarcoma, supplied by Sigma-Aldrich). Culture medium
504 was supplemented with 20% FCS, 2% non-essential amino acids and 5 µg/ml gentamicin. 1
505 ng/ml human fibroblast growth factor (FGF) (Sigma-Aldrich) and 4 µg/ml puromycin (Gibco)
506 were added for the first 48 h of culture. Afterwards, the medium was changed to puromycin-
507 free medium supplemented with FGF and was changed every other day.

508

509 *Leukocyte cell isolation from CNS for flow cytometry*

510 CNS tissue was dissected from mice transcardially perfused with 0.9% NaCl solution (Sigma-
511 Aldrich) and digested with 2 mg/ml collagenase II (Gibco) and 25 µg/ml DNase I (Roche) for 20
512 min at 37 °C and subsequently homogenized with a 18-G needle. Cells were then separated
513 using a 70–37–30% Percoll (Sigma-Aldrich) gradient centrifugation for 40 min, 500×g at 16 °C.
514 Cells at the 70/37% interphase were carefully collected and washed in PBS/FCS prior to 10 min
515 centrifugation at 500×g. To characterize MOG-specific T cells and cytokine production, cells
516 were plated in 96-well U-bottom plates and re-activated with 20 µg/ml MOG₃₅₋₅₅ peptide in
517 the presence of brefeldin A (Sigma-Aldrich) in T cell medium for 6 h at 37 °C. Afterwards, cells
518 were harvested and stained for flow cytometry analysis.

519

520 *Endothelial cell isolation for flow cytometry*

521 For CNS EC-isolation, mice were sacrificed and transcardially perfused as described above. The
522 dissected CNS tissue was digested with 2 mg/ml papain (Sigma-Aldrich) solution containing 25
523 µg/ml DNase I (Roche) for 30 min at 37 °C. During incubation, tissue was mechanically
524 homogenized using the gentleMACS™ Dissociator (Miltenyi). The resulting cell suspension was
525 filtered through a 70 µm cell strainer and centrifuged with a 22 % Percoll gradient for 30 min,
526 300×g at 15 °C. The pellet was used for flow cytometry staining.

527

528 *Flow cytometry analysis*

529 Before antibody staining, Fc receptors were blocked for 20 min using Fc-block (5 µg/ml)
530 (BioXCell). Single cell suspensions were stained for 30 min at 4 °C with antibodies against CD4
531 PerCP (GK1.5, rat monoclonal, 1:500, BioLegend), CD45 BV510 (30-F11, rat monoclonal, 1:200,
532 BioLegend), CD45.1 FITC (A20, mouse monoclonal, 1:1000, BioLegend), CD11b PECy7 (M1/70,
533 rat monoclonal, 1:1000, eBioscience™), Ly6C V450 (AL-21, rat monoclonal, 1:300 BD
534 Bioscience), Ly6C PerCP (HK1.4, rat monoclonal, 1:100, BioLegend), Ly6G PE (1A8, rat
535 monoclonal, 1:1000, BioLegend), CD11c APC (HL3, rat monoclonal, 1:800 BD Bioscience), CD19
536 PerCP (6D5, rat monoclonal, 1:400, BioLegend), TCRβ APC (H57-597, rat monoclonal, 1:1000,
537 BioLegend), CD31 PE (MEC 13.3, rat monoclonal, 1:100, BioLegend), CD31 PerCP-Cy5.5 (390,
538 rat monoclonal, 1:100, BioLegend), ICAM-1 APC (YN1/1.7.4, rat monoclonal, 1:300,
539 BioLegend), VCAM-1 PE-Cy7 (429 (MVCAM.A), rat monoclonal, 1:500, BioLegend), ICOSL
540 (CD275) PE (HK5.3, rat monoclonal, 1:100, BioLegend).

541 Afterwards, where indicated, cells were fixed and permeabilized with Cytofix/Cytoperm (BD
542 Bioscience) or Foxp3/Transcription Factor Staining Buffer Set (eBioscience™) and stained

543 overnight at 4 °C with intracellular antibodies. To specifically gate on MOG-specific cells, cells
544 were stained with anti-CD154 (CD40L) APC (MR1, hamster monoclonal, 1:200, BioLegend) and
545 cytokine production was assessed by staining with IL-17A eFl450 (eBio17B7, rat monoclonal,
546 1:300, eBioscience™), IFN- γ PE-Cy7 (XMG1.2, rat monoclonal, 1:1000, eBioscience™) and
547 GM-CSF PE (MP1-22E9, rat monoclonal, 1:200, eBioscience™). Staining for Foxp3 was
548 performed with Foxp3-FITC (FJK-16s, rat monoclonal, 1:200, eBioscience™).

549 Cells were acquired with a FACSCanto II cytometer (BD Bioscience) using FACS Diva software
550 (BD Bioscience). Flow cytometry data was analyzed with FlowJo™ software version 10 (BD
551 Bioscience). For all analyses, doublets (FSC and SSC properties) and dead cells (dye inclusion,
552 fixable viability dye APC-ef780 eBioscience™) were excluded.

553

554 *Fluorescence activated cell sorting (FACS) of CNS-ECs*

555 Endothelial cells from the spinal cord were isolated and subsequently stained with a surface
556 marker antibody panel and directly acquired at a FACS Aria III (BD Bioscience) with a 100 μ m
557 nozzle.

558

559 *RNA isolation and RNA sequencing*

560 For RNA sequencing 500 cells were sorted into lysis buffer and full-length cDNA was
561 synthesized using the SMART-Seq® v4 Ultra® Low Input Kit (TakaraBio). 1 ng of the resulting
562 cDNA was used for library preparation (Illumina Nextera XT DNA Library Prep Kit) according to
563 the manufacturer's instructions. Quantity was assessed using Invitrogen's Qubit HS assay kit
564 and library size was determined using Agilent's 2100 Bioanalyzer HS DNA assay. Barcoded
565 RNA-Seq libraries were onboard clustered using HiSeq® Rapid SR Cluster Kit v2 using 8pM and
566 59bps and were sequenced on the Illumina HiSeq2500 using HiSeq® Rapid SBS Kit v2 (59 Cycle).

567 The raw output data of the HiSeq was preprocessed according to the Illumina standard
568 protocol.

569

570 *RNA sequencing data analysis*

571 Quality control on the sequencing data was performed with the FastQC tool (version 0.11.8,
572 <https://www.bioinformatics.babraham.ac.uk/projects/fastqc/>). RNA sequencing reads were
573 aligned to the ENSEMBL Mus_musculus.GRCm38 reference genome. The corresponding
574 annotation (ENSEMBL v76) was retrieved from ENSEMBL FTP website. The STAR aligner
575 (version 2.6.1a) was used to perform mapping to the reference genome. Alignments were
576 processed with the featureCounts function of the Rsubread package (version 2.10.0), using
577 the annotation file also used for supporting the alignment. The exploration, modeling, and
578 interpretation of the expression data followed the protocols defined by Ludt *et. al* (2022) (88).
579 Exploratory data analysis was performed with the pcaExplorer package (version 2.22.0).
580 Differential expression analysis was performed with DESeq2 package (version 1.36.0), setting
581 the false discovery rate (FDR) cutoff to 0.05. Accurate estimation of the effect sizes (described
582 as log2 fold change) was performed using the apeglm shrinkage estimator (version 1.18.0).
583 Gene expression profiles were plotted as heatmaps (color-coded standardized z-scores for the
584 expression values, after regularized logarithm transformation) to enable comparison across
585 samples, created with the GeneTonic package (version 2.0.3) (89). For functional annotation
586 of Gene Ontology (GO) and analysis of KEGG pathway enrichment, the web-based DAVID 2021
587 tool was used.

588

589 *FITC-dextran permeability assay*

590 FITC-dextran (avg. mol. weight 3,000-5,000 Da, Sigma-Aldrich) was dissolved at 2 mM in PBS.
591 100 µl of this stock solution was injected i.p. into the mice. After 15 min, mice were sacrificed
592 and perfused with 0.9% NaCl solution. Spinal cords and half brains were weighed and
593 subsequently homogenized in 200 µl (spinal cord) or 500 µl (half brain) PBS in metal bead
594 lysing matrix tubes (MP Biomedicals) using the FastPrep-24™ (MP Biomedicals) system. Tubes
595 were centrifuged at 15,000 x g for 20 min at 4°C and 100 µl of the supernatant were
596 transferred into a 96 well flat black plate (Greiner). FITC fluorescence was measured with a
597 Spark plate reader (Tecan) with an excitation of 490/10 nm and an emission of 520/10 nm and
598 raw fluorescence units (RFU) were normalized to tissue weights.

599

600 *RNA isolation from pMBMECs and real time (RT) PCR*

601 Isolation of RNA from cultured pMBMECs was performed with the ReliaPrep™ RNA Cell
602 Miniprep System (Promega) following manufacturers guidelines. RNA concentrations were
603 determined by measuring absorbance using the NanoQuant Plate™ (Tecan) at an Infinite
604 M200 pro plate reader (Tecan). cDNA was synthesized using 200–1000 ng of total RNA with
605 the QuantiTect® Reverse Transcription Kit (Qiagen) and subsequently used for qPCR, which
606 was performed with the StepOnePlus™ Real-Time PCR System (Life Technologies) using SYBR
607 Green reagent (Promega). Fold enrichment was calculated using the Delta–Delta CT method
608 normalized to hypoxanthin-guanin-phosphoribosyltransferase (*Hprt*) as house-keeping
609 reference. *Tnfaip3* primer were ordered as QuantiTect Primer Assay (QT00134064, Qiagen).
610 *Icosl* primer (forward: 5'- AGGCTCCCTGGACATCTCG -3'; reverse: 5'-
611 CAGTACAGCAAGGACGGGGA -3') were self-designed using primer-BLAST tool from the
612 National Center for Biotechnology Information (NCBI) and were synthesized by Metabion.

613

614 *Western blot*

615 Western blotting for the A20 protein was performed on primary brain endothelial cells of
616 A20^{fl/fl} and A20^{ACNS-EC} mice. After reaching confluence, cells were lysed and western blotting
617 was performed as described before (22) using antibodies targeting A20 (A-12, mouse
618 monoclonal, Santa Cruz, 1:500) and actin (C-11, goat polyclonal, Santa Cruz, 1:1000) and
619 secondary antibodies against mouse IgG (HRP-coupled, Santa Cruz, 1:1000) and goat IgG (HRP-
620 coupled, DAKO, 1:10000), respectively.

621

622 *In vitro T cell static adhesion assay*

623

624 pMBMECs were isolated and cultured as described above for 7 days on μ -dishes (ibidi GmbH).
625 After 4 days, cells were stimulated with 20 ng/ml IL-1 β for 72 h. Th1 or Th17 cells from 2D2
626 C57BL/6 mice were thawed and rested for approximately 4 h in T cell medium and
627 subsequently labelled with 1 μ M CellTrackerTM Green (Thermo Fisher Scientific) for 30 min.
628 pMBMECs were incubated with 15 μ g/ml anti-mouse ICOSL (HK5.3, rat IgG2a monoclonal,
629 BioXCell) or 15 μ g/ml negative control (MJ7/18, rat IgG2a anti mouse endoglin (76)) for 30
630 min. 100,000 T cells were added to the pMBMECs and were allowed to adhere for 30 min on
631 a shaking platform. Wells were washed with PBS and fixed with 1% PFA for 10 min before
632 mounting on glass slides with DAPI. Images were acquired at an Eclipse E600 microscope
633 (Nikon) and adhering T cells were counted using ImageJ software (National Institute of
634 Health).

635

636 *In vitro T cell migration assay under physiological flow*

637 In vitro live-cell imaging of T cell diapedesis across pMBMECs was performed as described
638 before (90). In brief, pMBMECs were isolated and cultured for 7 days on μ -dishes (ibidi GmbH).
639 After 4 days, cells were stimulated with 20 ng/mL IL-1 β for 72 h. 2D2 Th1 cells were
640 resuspended at 1×10^6 cells/ml in T cell medium. Prior to the experiment, pMBMECs were

641 treated with 15 $\mu\text{g}/\text{ml}$ anti-mouse ICOSL (HK5.3, rat IgG2a monoclonal, BioXCell) or 15 $\mu\text{g}/\text{ml}$
642 negative control (MJ7/18, rat IgG2a anti mouse endoglin (76)) for 30 min at 37°C.
643 Accumulation of 2D2 Th1 on pMBMECs in the flow chamber was allowed for 4 min at a low
644 shear (0.1 dyn/cm^2), followed by physiological shear (1.5 dyn/cm^2) for an additional 20 min,
645 for a total recording time of 24 min. Image acquisition was performed at 10 \times magnification
646 with the AxioObserver inverted microscope (Carl Zeiss) with differential interference contrast
647 using the camera Evolve Delta (Teledyne Photometrics). Image frames were recorded every
648 10 s. Image analysis was performed using ImageJ software (National Institute of Health). T cell
649 post-arrest behavior was defined and expressed as described previously (91). T cell crawling
650 tracks were evaluated after manual tracking of individual T cells using the manual tracking
651 plug-in of ImageJ. Distance and speed of crawling tracks were evaluated using chemotaxis and
652 migration tool (version 2.0, Ibidi GmbH).

653

654 *Adeno-associated virus (AAV) design and applications*

655 For knockdown of ICOSL specifically in CNS-ECs AAV-BR1 (45) was used to deliver a short
656 hairpin (sh) RNA against *Icosl* carrying the sense sequence GCAGAAAGTTTCACTGGAAATCTC
657 to the target cells. The AAV-BR1-RSV-GFP-H1-shRNA_*Icosl* and the control AAV-BR1-RSV-GFP-
658 H1-shRNA_scrambled constructs were produced by the Viral Vector Production Unit of the
659 Universitat Autònoma Barcelona, Spain. The AAVs were delivered to us ready for use.

660 For in vitro experiments, pMBMECs grown in 48-well plates were transfected with 0.6×10^6
661 genomic particles (gp) per well four days after seeding. For in vivo experiments, constructs
662 were delivered i.v. at a concentration of 1.8×10^{11} gp in 100 μl sterile PBS. AAV-BR1-eGFP was
663 used as described elsewhere (45).

664

665 *Statistics*

666 Statistical analyses were performed with Prism v9 software (GraphPad). All values are
667 represented as mean \pm standard error of the mean (SEM) unless otherwise stated. *P* values
668 were considered significant with $p < 0.05$.

669

670 *Study approval*

671 All animal experiments were approved by the local administrations (Landesuntersuchungsamt
672 Koblenz, Germany; Ministerium für Energiewende, Landwirtschaft, Umwelt und ländliche
673 Räume, Kiel, Germany; individual approval numbers G20-1-049 and G22-1-005). Experiments
674 were performed in accordance with the guidelines from the translational animal research
675 center (TARC) Mainz, Germany. All efforts were made to minimize suffering of the mice.

676

677 *Data availability*

678 The RNA-seq data presented in this manuscript have been deposited in the Gene Expression
679 Omnibus (GEO) under accession number GSE221318. All other data is available in the
680 'Supporting data values' file.

681

682 AUTHOR CONTRIBUTIONS

683 L.J. performed experiments, analyzed data, prepared figures, and wrote the manuscript. S.S.,
684 K.M., J.L., M.A.K., J.C.A., and J.W. performed experiments and analyzed data; F.M. performed
685 bioinformatic analysis; N.R., I.P. and C.S. helped with experiments, data analysis and
686 discussion. E.S. helped with experiments and manuscript writing. M.K. and T.B. provided
687 reagents and guided preparation of samples for RNA seq. K.K. helped with histology and
688 confocal imaging. M.H.H.S., D.S. and G.v.L. provided mouse strains. J.K. provided the AAV-BR1

689 plasmid. B.E. and M.S. were associated with conceptualization and supervision of the project,
690 funding acquisition, and finalization of the manuscript. A.W. supervised the project, acquired
691 funding and wrote the manuscript together with L.J.

692

693 ACKNOWLEDGEMENTS

694 We would like to thank Ralf Adams for allowing us to use the Cdh5-CreER^{T2} mice. We further
695 thank Sara Barcos for excellent technical assistance and Dr. Natalia Soshnikova for helping
696 with cDNA preparation for sequencing. We would like to thank Dr. Tommy Regen, Katlynn
697 Carter, Rebecca Jasser, Elisa Blickberndt and Michaela Blanfeld for helping with the
698 experiments. Work was supported by the computing infrastructure provided by the Core
699 Facility Bioinformatics and the Core Facility Flow Cytometry (CFFC) at the University Medical
700 Center Mainz. Graphical abstract was created with BioRender.com.

701 This work was funded by the Deutsche Forschungsgemeinschaft (DFG, German Research
702 Foundation) project number 318346496 – SFB1292/2 to F.M., T.B., A.W., and project number
703 490846870 – TRR355/1 to A.W. and T.B. and SCHW 416/5-3 to M.S. This work was further
704 funded with an unrestricted grant from Roche Global Neuroscience, Basel, Switzerland.

705

706 REFERENCES

- 707 1. Multiple-Sclerosis-International-Federation. The Atlas of MS. 2022.
 708 <https://www.msif.org/news/2021/04/27/the-atlas-of-ms-part-2-goes-live/>
- 709 2. Baecher-Allan C, et al. Multiple Sclerosis: Mechanisms and Immunotherapy. *Neuron*.
 710 Feb 21 2018;97(4):742-768. doi:10.1016/j.neuron.2018.01.021
- 711 3. Lassmann H. Multiple Sclerosis Pathology. *Cold Spring Harb Perspect Med*. Mar 1
 712 2018;8(3)doi:10.1101/cshperspect.a028936
- 713 4. Waisman A, Johann L. Antigen-presenting cell diversity for T cell reactivation in
 714 central nervous system autoimmunity. *J Mol Med (Berl)*. Dec 2018;96(12):1279-1292.
 715 doi:10.1007/s00109-018-1709-7
- 716 5. Engelhardt B, et al. Vascular, glial, and lymphatic immune gateways of the central
 717 nervous system. *Acta Neuropathol*. Sep 2016;132(3):317-38. doi:10.1007/s00401-016-1606-
 718 5
- 719 6. Engelhardt B, Ransohoff RM. Capture, crawl, cross: the T cell code to breach the
 720 blood-brain barriers. *Trends Immunol*. Dec 2012;33(12):579-89. doi:10.1016/j.it.2012.07.004
- 721 7. Engelhardt B, et al. The movers and shapers in immune privilege of the CNS. *Nat*
 722 *Immunol*. Feb 2017;18(2):123-131. doi:10.1038/ni.3666
- 723 8. Lou J, et al. Direct cell/cell contact with stimulated T lymphocytes induces the
 724 expression of cell adhesion molecules and cytokines by human brain microvascular
 725 endothelial cells. *Eur J Immunol*. Dec 1996;26(12):3107-13. doi:10.1002/eji.1830261242
- 726 9. Carrithers MD, et al. Differential adhesion molecule requirements for immune
 727 surveillance and inflammatory recruitment. *Brain*. Jun 2000;123 (Pt 6):1092-101.
 728 doi:10.1093/brain/123.6.1092
- 729 10. Munji RN, et al. Profiling the mouse brain endothelial transcriptome in health and
 730 disease models reveals a core blood-brain barrier dysfunction module. *Nat Neurosci*. Nov
 731 2019;22(11):1892-1902. doi:10.1038/s41593-019-0497-x
- 732 11. Profaci CP, et al. The blood-brain barrier in health and disease: Important
 733 unanswered questions. *J Exp Med*. Apr 6 2020;217(4)doi:10.1084/jem.20190062
- 734 12. Jeong HW, et al. Single-cell transcriptomics reveals functionally specialized vascular
 735 endothelium in brain. *Elife*. Oct 5 2022;11doi:10.7554/eLife.57520
- 736 13. Hauptmann J, et al. Interleukin-1 promotes autoimmune neuroinflammation by
 737 suppressing endothelial heme oxygenase-1 at the blood-brain barrier. *Acta Neuropathol*. Oct
 738 2020;140(4):549-567. doi:10.1007/s00401-020-02187-x
- 739 14. Thornton P, et al. Interleukin-1 drives cerebrovascular inflammation via MAP kinase-
 740 independent pathways. *Curr Neurovasc Res*. Nov 2010;7(4):330-40.
 741 doi:10.2174/156720210793180800
- 742 15. Ledebur HC, Parks TP. Transcriptional regulation of the intercellular adhesion
 743 molecule-1 gene by inflammatory cytokines in human endothelial cells. Essential roles of a
 744 variant NF-kappa B site and p65 homodimers. *J Biol Chem*. Jan 13 1995;270(2):933-43.
 745 doi:10.1074/jbc.270.2.933
- 746 16. Wertheimer SJ, et al. Intercellular adhesion molecule-1 gene expression in human
 747 endothelial cells. Differential regulation by tumor necrosis factor-alpha and phorbol
 748 myristate acetate. *J Biol Chem*. Jun 15 1992;267(17):12030-5.
- 749 17. Neish AS, et al. Functional analysis of the human vascular cell adhesion molecule 1
 750 promoter. *J Exp Med*. Dec 1 1992;176(6):1583-93. doi:10.1084/jem.176.6.1583

- 751 18. Shu HB, et al. Differential regulation of vascular cell adhesion molecule 1 gene
752 expression by specific NF-kappa B subunits in endothelial and epithelial cells. *Mol Cell Biol.*
753 Oct 1993;13(10):6283-9. doi:10.1128/mcb.13.10.6283-6289.1993
- 754 19. Tripathi AK, et al. Plasmodium falciparum-infected erythrocytes induce NF-kappaB
755 regulated inflammatory pathways in human cerebral endothelium. *Blood.* Nov 5
756 2009;114(19):4243-52. doi:10.1182/blood-2009-06-226415
- 757 20. Jacob A, et al. C5a/CD88 signaling alters blood-brain barrier integrity in lupus through
758 nuclear factor-kappaB. *J Neurochem.* Dec 2011;119(5):1041-51. doi:10.1111/j.1471-
759 4159.2011.07490.x
- 760 21. Kielland A, et al. NF-kappaB activity in perinatal brain during infectious and hypoxic-
761 ischemic insults revealed by a reporter mouse. *Brain Pathol.* Jul 2012;22(4):499-510.
762 doi:10.1111/j.1750-3639.2011.00548.x
- 763 22. Ridder DA, et al. Brain endothelial TAK1 and NEMO safeguard the neurovascular unit.
764 *J Exp Med.* Sep 21 2015;212(10):1529-49. doi:10.1084/jem.20150165
- 765 23. Opipari AW, Jr., et al. The A20 zinc finger protein protects cells from tumor necrosis
766 factor cytotoxicity. *J Biol Chem.* Jun 25 1992;267(18):12424-7.
- 767 24. Cooper JT, et al. A20 blocks endothelial cell activation through a NF-kappaB-
768 dependent mechanism. *J Biol Chem.* Jul 26 1996;271(30):18068-73.
769 doi:10.1074/jbc.271.30.18068
- 770 25. Tewari M, et al. Lymphoid expression and regulation of A20, an inhibitor of
771 programmed cell death. *J Immunol.* Feb 15 1995;154(4):1699-706.
- 772 26. International Multiple Sclerosis Genetics C, et al. Analysis of immune-related loci
773 identifies 48 new susceptibility variants for multiple sclerosis. *Nat Genet.* Nov
774 2013;45(11):1353-60. doi:10.1038/ng.2770
- 775 27. Guedes RP, et al. A20 deficiency causes spontaneous neuroinflammation in mice. *J*
776 *Neuroinflammation.* Jul 16 2014;11:122. doi:10.1186/1742-2094-11-122
- 777 28. Wang X, et al. Astrocytic A20 ameliorates experimental autoimmune
778 encephalomyelitis by inhibiting NF-kappaB- and STAT1-dependent chemokine production in
779 astrocytes. *Acta Neuropathol.* Nov 2013;126(5):711-724. doi:10.1007/s00401-013-1183-9
- 780 29. Voet S, et al. A20 critically controls microglia activation and inhibits inflammasome-
781 dependent neuroinflammation. *Nat Commun.* May 23 2018;9(1):2036. doi:10.1038/s41467-
782 018-04376-5
- 783 30. Mohebiany AN, et al. Microglial A20 Protects the Brain from CD8 T-Cell-Mediated
784 Immunopathology. *Cell Rep.* Feb 4 2020;30(5):1585-1597 e6.
785 doi:10.1016/j.celrep.2019.12.097
- 786 31. Zhang Y, et al. An RNA-sequencing transcriptome and splicing database of glia,
787 neurons, and vascular cells of the cerebral cortex. *J Neurosci.* Sep 3 2014;34(36):11929-47.
788 doi:10.1523/JNEUROSCI.1860-14.2014
- 789 32. Ridder DA, et al. TAK1 in brain endothelial cells mediates fever and lethargy. *J Exp*
790 *Med.* Dec 19 2011;208(13):2615-23. doi:10.1084/jem.20110398
- 791 33. Wang Y, et al. Ephrin-B2 controls VEGF-induced angiogenesis and lymphangiogenesis.
792 *Nature.* May 27 2010;465(7297):483-6. doi:10.1038/nature09002
- 793 34. Koutrolos M, et al. Treg cells mediate recovery from EAE by controlling effector T cell
794 proliferation and motility in the CNS. *Acta Neuropathol Commun.* Dec 5 2014;2:163.
795 doi:10.1186/s40478-014-0163-1
- 796 35. Brown WR. A review of string vessels or collapsed, empty basement membrane
797 tubes. *J Alzheimers Dis.* 2010;21(3):725-39. doi:10.3233/JAD-2010-100219

- 798 36. Abadier M, et al. Cell surface levels of endothelial ICAM-1 influence the transcellular
799 or paracellular T-cell diapedesis across the blood-brain barrier. *Eur J Immunol.* Apr
800 2015;45(4):1043-58. doi:10.1002/eji.201445125
- 801 37. Polman CH, et al. A randomized, placebo-controlled trial of natalizumab for relapsing
802 multiple sclerosis. *N Engl J Med.* Mar 2 2006;354(9):899-910. doi:10.1056/NEJMoa044397
- 803 38. Rudick RA, et al. Natalizumab plus interferon beta-1a for relapsing multiple sclerosis.
804 *N Engl J Med.* Mar 2 2006;354(9):911-23. doi:10.1056/NEJMoa044396
- 805 39. Havrdova E, et al. Effect of natalizumab on clinical and radiological disease activity in
806 multiple sclerosis: a retrospective analysis of the Natalizumab Safety and Efficacy in
807 Relapsing-Remitting Multiple Sclerosis (AFFIRM) study. *Lancet Neurol.* Mar 2009;8(3):254-60.
808 doi:10.1016/S1474-4422(09)70021-3
- 809 40. Bloomgren G, et al. Risk of natalizumab-associated progressive multifocal
810 leukoencephalopathy. *N Engl J Med.* May 17 2012;366(20):1870-80.
811 doi:10.1056/NEJMoa1107829
- 812 41. Caravagna C, et al. Diversity of innate immune cell subsets across spatial and
813 temporal scales in an EAE mouse model. *Sci Rep.* Mar 23 2018;8(1):5146.
814 doi:10.1038/s41598-018-22872-y
- 815 42. Hovelmeyer N, et al. A20 deficiency in B cells enhances B-cell proliferation and results
816 in the development of autoantibodies. *Eur J Immunol.* Mar 2011;41(3):595-601.
817 doi:10.1002/eji.201041313
- 818 43. Khayyamian S, et al. ICOS-ligand, expressed on human endothelial cells, costimulates
819 Th1 and Th2 cytokine secretion by memory CD4+ T cells. *Proc Natl Acad Sci U S A.* Apr 30
820 2002;99(9):6198-203. doi:10.1073/pnas.092576699
- 821 44. Wheway J, et al. The brain microvascular endothelium supports T cell proliferation
822 and has potential for alloantigen presentation. *PLoS One.* 2013;8(1):e52586.
823 doi:10.1371/journal.pone.0052586
- 824 45. Korbelin J, et al. A brain microvasculature endothelial cell-specific viral vector with
825 the potential to treat neurovascular and neurological diseases. *EMBO Mol Med.* Jun
826 2016;8(6):609-25. doi:10.15252/emmm.201506078
- 827 46. Ansari AM, et al. Cellular GFP Toxicity and Immunogenicity: Potential Confounders in
828 in Vivo Cell Tracking Experiments. *Stem Cell Rev Rep.* Oct 2016;12(5):553-559.
829 doi:10.1007/s12015-016-9670-8
- 830 47. Barclay AN. Membrane proteins with immunoglobulin-like domains--a master
831 superfamily of interaction molecules. *Semin Immunol.* Aug 2003;15(4):215-23.
832 doi:10.1016/s1044-5323(03)00047-2
- 833 48. Lecuyer MA, et al. Dual role of ALCAM in neuroinflammation and blood-brain barrier
834 homeostasis. *Proc Natl Acad Sci U S A.* Jan 24 2017;114(4):E524-E533.
835 doi:10.1073/pnas.1614336114
- 836 49. Michel L, et al. Activated leukocyte cell adhesion molecule regulates B lymphocyte
837 migration across central nervous system barriers. *Sci Transl Med.* Nov 13
838 2019;11(518)doi:10.1126/scitranslmed.aaw0475
- 839 50. Laroche C, et al. Melanoma cell adhesion molecule identifies encephalitogenic T
840 lymphocytes and promotes their recruitment to the central nervous system. *Brain.* Oct
841 2012;135(Pt 10):2906-24. doi:10.1093/brain/aws212
- 842 51. Laroche C, et al. Melanoma cell adhesion molecule-positive CD8 T lymphocytes
843 mediate central nervous system inflammation. *Ann Neurol.* Jul 2015;78(1):39-53.
844 doi:10.1002/ana.24415

- 845 52. Charabati M, et al. DICAM promotes TH17 lymphocyte trafficking across the blood-
846 brain barrier during autoimmune neuroinflammation. *Sci Transl Med*. Jan 5
847 2022;14(626):eabj0473. doi:10.1126/scitranslmed.abj0473
- 848 53. Du F, et al. Inflammatory Th17 Cells Express Integrin alphavbeta3 for Pathogenic
849 Function. *Cell Rep*. Aug 2 2016;16(5):1339-1351. doi:10.1016/j.celrep.2016.06.065
- 850 54. Koh KH, et al. Nonimmune cell-derived ICOS ligand functions as a renoprotective
851 alphavbeta3 integrin-selective antagonist. *J Clin Invest*. Apr 1 2019;129(4):1713-1726.
852 doi:10.1172/JCI123386
- 853 55. Dopp JM, et al. Expression of ICAM-1, VCAM-1, L-selectin, and leukosialin in the
854 mouse central nervous system during the induction and remission stages of experimental
855 allergic encephalomyelitis. *J Neuroimmunol*. Oct 1994;54(1-2):129-44. doi:10.1016/0165-
856 5728(94)90239-9
- 857 56. Lee SJ, Benveniste EN. Adhesion molecule expression and regulation on cells of the
858 central nervous system. *J Neuroimmunol*. Aug 3 1999;98(2):77-88. doi:10.1016/s0165-
859 5728(99)00084-3
- 860 57. Alvarez JI, et al. Disruption of central nervous system barriers in multiple sclerosis.
861 *Biochim Biophys Acta*. Feb 2011;1812(2):252-64. doi:10.1016/j.bbadis.2010.06.017
- 862 58. Larochelle C, et al. How do immune cells overcome the blood-brain barrier in
863 multiple sclerosis? *FEBS Lett*. Dec 1 2011;585(23):3770-80.
864 doi:10.1016/j.febslet.2011.04.066
- 865 59. Merrill JE, Murphy SP. Inflammatory events at the blood brain barrier: regulation of
866 adhesion molecules, cytokines, and chemokines by reactive nitrogen and oxygen species.
867 *Brain Behav Immun*. Dec 1997;11(4):245-63. doi:10.1006/brbi.1997.0496
- 868 60. O'Carroll SJ, et al. Pro-inflammatory TNFalpha and IL-1beta differentially regulate the
869 inflammatory phenotype of brain microvascular endothelial cells. *J Neuroinflammation*. Jul 8
870 2015;12:131. doi:10.1186/s12974-015-0346-0
- 871 61. Levesque SA, et al. Myeloid cell transmigration across the CNS vasculature triggers IL-
872 1beta-driven neuroinflammation during autoimmune encephalomyelitis in mice. *J Exp Med*.
873 May 30 2016;213(6):929-49. doi:10.1084/jem.20151437
- 874 62. Saitou M, et al. Occludin-deficient embryonic stem cells can differentiate into
875 polarized epithelial cells bearing tight junctions. *J Cell Biol*. Apr 20 1998;141(2):397-408.
876 doi:10.1083/jcb.141.2.397
- 877 63. Saitou M, et al. Complex phenotype of mice lacking occludin, a component of tight
878 junction strands. *Mol Biol Cell*. Dec 2000;11(12):4131-42. doi:10.1091/mbc.11.12.4131
- 879 64. Yu AS, et al. Knockdown of occludin expression leads to diverse phenotypic
880 alterations in epithelial cells. *Am J Physiol Cell Physiol*. Jun 2005;288(6):C1231-41.
881 doi:10.1152/ajpcell.00581.2004
- 882 65. Schulzke JD, et al. Epithelial transport and barrier function in occludin-deficient mice.
883 *Biochim Biophys Acta*. May 15 2005;1669(1):34-42. doi:10.1016/j.bbamem.2005.01.008
- 884 66. Daems CSMVVvLGDHRC-VZCP. A20/TNFAIP3 heterozygosity predisposes to
885 behavioral symptoms in a mouse model for neuropsychiatric lupus. *Brain, Behavior, &*
886 *Immunity - Health*. 2020;
- 887 67. Gelderblom M, et al. Neutralization of the IL-17 axis diminishes neutrophil invasion
888 and protects from ischemic stroke. *Blood*. Nov 1 2012;120(18):3793-802. doi:10.1182/blood-
889 2012-02-412726
- 890 68. Liesz A, et al. Inhibition of lymphocyte trafficking shields the brain against deleterious
891 neuroinflammation after stroke. *Brain*. Mar 2011;134(Pt 3):704-20.
892 doi:10.1093/brain/awr008

893 69. Neumann J, et al. Very-late-antigen-4 (VLA-4)-mediated brain invasion by neutrophils
894 leads to interactions with microglia, increased ischemic injury and impaired behavior in
895 experimental stroke. *Acta Neuropathol.* Feb 2015;129(2):259-77. doi:10.1007/s00401-014-
896 1355-2

897 70. Lyck R, et al. ALCAM (CD166) is involved in extravasation of monocytes rather than T
898 cells across the blood-brain barrier. *J Cereb Blood Flow Metab.* Aug 2017;37(8):2894-2909.
899 doi:10.1177/0271678X16678639

900 71. Schneider-Hohendorf T, et al. VLA-4 blockade promotes differential routes into
901 human CNS involving PSGL-1 rolling of T cells and MCAM-adhesion of TH17 cells. *J Exp Med.*
902 Aug 25 2014;211(9):1833-46. doi:10.1084/jem.20140540

903 72. Charabati M, et al. MCAM+ brain endothelial cells contribute to neuroinflammation
904 by recruiting pathogenic CD4+ T lymphocytes. *Brain.* Apr 19 2023;146(4):1483-1495.
905 doi:10.1093/brain/awac389

906 73. Roussel L, et al. Loss of human ICOSL results in combined immunodeficiency. *J Exp*
907 *Med.* Dec 3 2018;215(12):3151-3164. doi:10.1084/jem.20180668

908 74. Schlager C, et al. Effector T-cell trafficking between the leptomeninges and the
909 cerebrospinal fluid. *Nature.* Feb 18 2016;530(7590):349-53. doi:10.1038/nature16939

910 75. Bartholomaeus I, et al. Effector T cell interactions with meningeal vascular structures
911 in nascent autoimmune CNS lesions. *Nature.* Nov 5 2009;462(7269):94-8.
912 doi:10.1038/nature08478

913 76. Engelhardt B, et al. The development of experimental autoimmune
914 encephalomyelitis in the mouse requires alpha4-integrin but not alpha4beta7-integrin. *J Clin*
915 *Invest.* Dec 15 1998;102(12):2096-105. doi:10.1172/JCI4271

916 77. Dong C, et al. ICOS co-stimulatory receptor is essential for T-cell activation and
917 function. *Nature.* Jan 4 2001;409(6816):97-101. doi:10.1038/35051100

918 78. Mak TW, et al. Costimulation through the inducible costimulator ligand is essential
919 for both T helper and B cell functions in T cell-dependent B cell responses. *Nat Immunol.* Aug
920 2003;4(8):765-72. doi:10.1038/ni947

921 79. Coyle AJ, et al. The CD28-related molecule ICOS is required for effective T cell-
922 dependent immune responses. *Immunity.* Jul 2000;13(1):95-105. doi:10.1016/s1074-
923 7613(00)00011-x

924 80. Rottman JB, et al. The costimulatory molecule ICOS plays an important role in the
925 immunopathogenesis of EAE. *Nat Immunol.* Jul 2001;2(7):605-11. doi:10.1038/89750

926 81. Galicia G, et al. ICOS deficiency results in exacerbated IL-17 mediated experimental
927 autoimmune encephalomyelitis. *J Clin Immunol.* Jul 2009;29(4):426-33. doi:10.1007/s10875-
928 009-9287-7

929 82. Vereecke L, et al. Enterocyte-specific A20 deficiency sensitizes to tumor necrosis
930 factor-induced toxicity and experimental colitis. *J Exp Med.* Jul 5 2010;207(7):1513-23.
931 doi:10.1084/jem.20092474

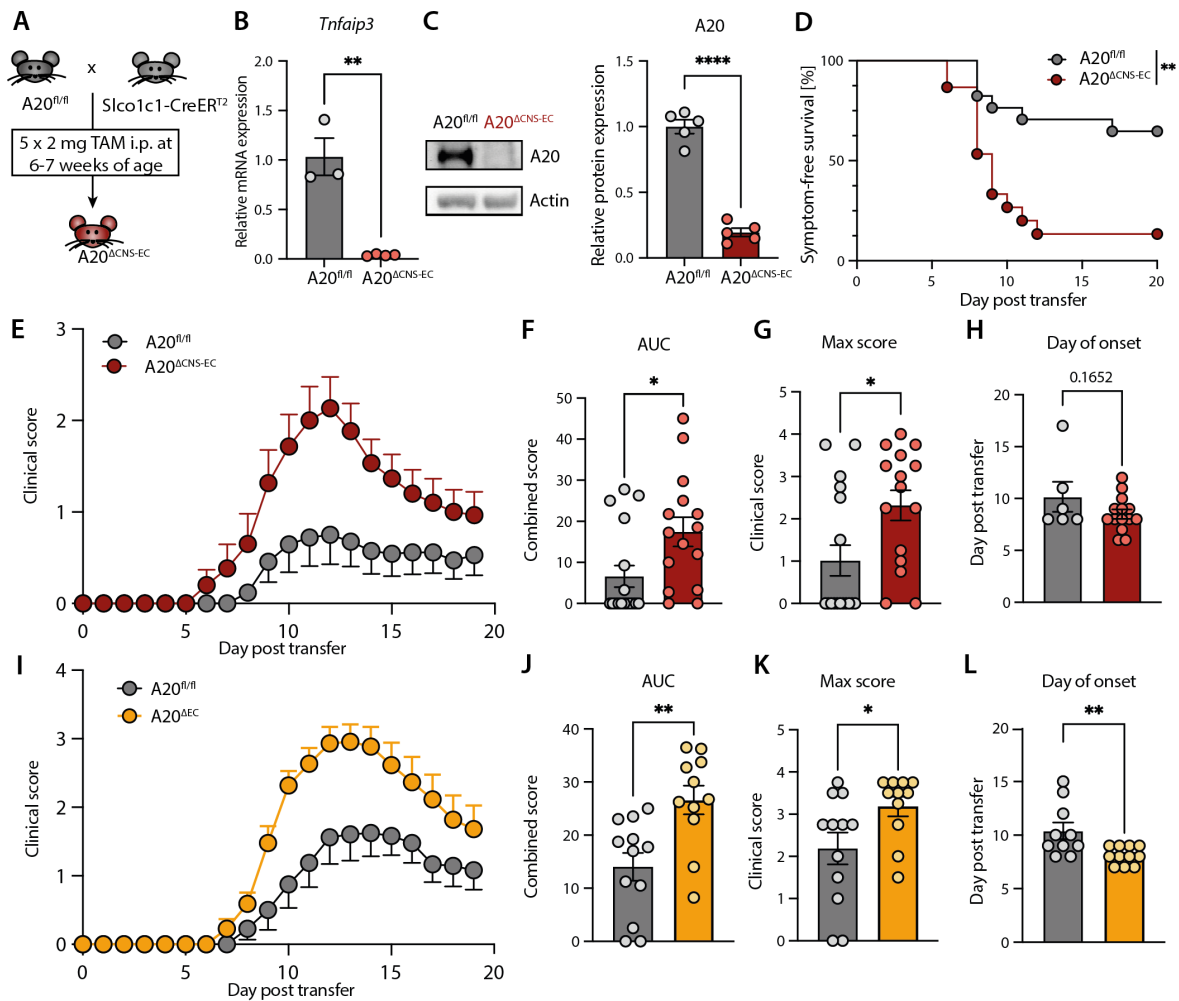
932 83. Srinivas S, et al. Cre reporter strains produced by targeted insertion of EYFP and ECFP
933 into the ROSA26 locus. *BMC Dev Biol.* 2001;1:4. doi:10.1186/1471-213x-1-4

934 84. Chen H, et al. Hydroxycarboxylic acid receptor 2 mediates dimethyl fumarate's
935 protective effect in EAE. *J Clin Invest.* May 2014;124(5):2188-92. doi:10.1172/JCI72151

936 85. Wenzel J, et al. Endogenous THBD (Thrombomodulin) Mediates Angiogenesis in the
937 Ischemic Brain-Brief Report. *Arterioscler Thromb Vasc Biol.* Dec 2020;40(12):2837-2844.
938 doi:10.1161/ATVBAHA.120.315061

- 939 86. Lubjuhn J, et al. Functional testing in a mouse stroke model induced by occlusion of
940 the distal middle cerebral artery. *J Neurosci Methods*. Oct 30 2009;184(1):95-103.
941 doi:10.1016/j.jneumeth.2009.07.029
- 942 87. Coisne C, et al. Mouse syngenic in vitro blood-brain barrier model: a new tool to
943 examine inflammatory events in cerebral endothelium. *Lab Invest*. Jun 2005;85(6):734-46.
944 doi:10.1038/labinvest.3700281
- 945 88. Ludt A, et al. Interactive and Reproducible Workflows for Exploring and Modeling
946 RNA-seq Data with pcaExplorer, Ideal, and GeneTonic. *Curr Protoc*. Apr 2022;2(4):e411.
947 doi:10.1002/cpz1.411
- 948 89. Marini F, et al. GeneTonic: an R/Bioconductor package for streamlining the
949 interpretation of RNA-seq data. *BMC Bioinformatics*. Dec 23 2021;22(1):610.
950 doi:10.1186/s12859-021-04461-5
- 951 90. Coisne C, et al. Live cell imaging techniques to study T cell trafficking across the
952 blood-brain barrier in vitro and in vivo. *Fluids Barriers CNS*. Jan 21 2013;10(1):7.
953 doi:10.1186/2045-8118-10-7
- 954 91. Marchetti L, et al. ACKR1 favors transcellular over paracellular T-cell diapedesis
955 across the blood-brain barrier in neuroinflammation in vitro. *Eur J Immunol*. Jan
956 2022;52(1):161-177. doi:10.1002/eji.202149238
957

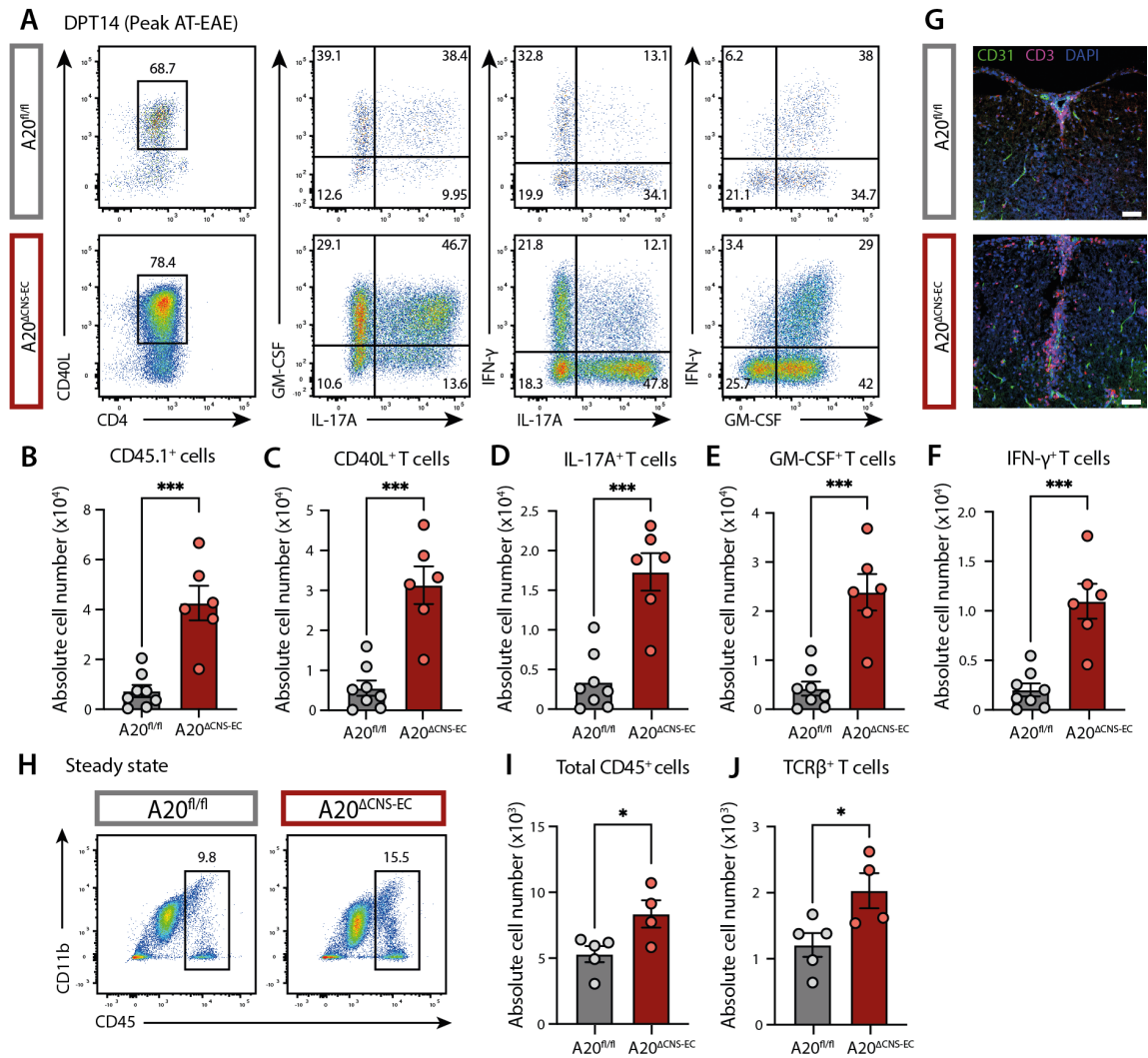
958



959
960

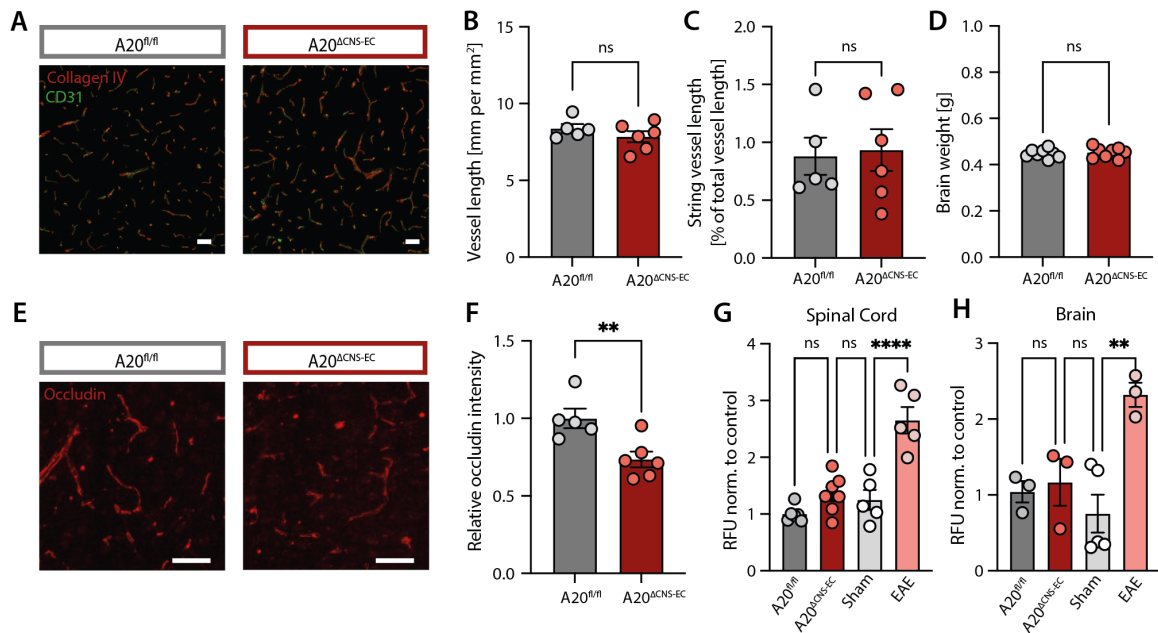
961 **Figure 1: CNS EC-A20 plays a protective role in CNS autoimmunity**

962 (A) Breeding strategy for generation of $A20^{\Delta CNS-EC}$ mice. Conditional deletion of *Tnfrap3* in
 963 $A20^{\Delta CNS-EC}$ mice is achieved through tamoxifen (TAM) injections. (B) Validation of *Tnfrap3*
 964 deletion in pMBMECs from $A20^{\Delta CNS-EC}$ mice by RT-PCR. *Tnfrap3* mRNA levels are presented
 965 relative to control (n = 3-4 mice per group). (C) Western blot analysis of A20 protein in cultured
 966 primary brain endothelial cells from $A20^{\Delta CNS-EC}$ and littermate control mice. Protein expression
 967 of A20 is normalized to actin levels and presented relative to the expression in controls (n = 5
 968 mice per group). (D-H) Adoptive transfer (AT)-EAE disease in $A20^{\Delta CNS-EC}$ mice and $A20^{fl/fl}$
 969 littermate. Clinical signs of EAE were monitored daily. Data is pooled from two independent
 970 experiments with n = 15-17 mice per group. (D) Probability of symptom-free survival is shown
 971 as Kaplan Meier curve. (E) Clinical signs of EAE are shown as mean clinical disease scores +/-
 972 SEM. (F) Area under the curve (AUC), (G) maximum clinical scores and (H) day of onset
 973 analyses of clinical course shown in (E). Every circle represents a single mouse. (I-L)
 974 AT-EAE disease was induced in $A20^{\Delta EC}$ lacking A20 in all endothelial cells driven by the *Cdh5-CreER^{T2}*
 975 and $A20^{fl/fl}$ littermate controls as described before. Clinical signs of EAE were monitored daily.
 976 Data is pooled from two independent experiments with n = 11-12 mice per group. (I) Clinical
 977 signs of EAE are shown as mean clinical disease scores +/- SEM. (J) AUC, (K) maximum clinical
 978 scores and (L) day of onset analyses of clinical course shown in (I). Every circle represents a
 979 single mouse. Statistical significance was determined by two-tailed unpaired Student's t-test
 980 (B, C, F-H, J-L) or Log-rank (Mantel-Cox) test (D). * p<0.05, ** p<0.01, **** p<0.0001.
 981



982
983

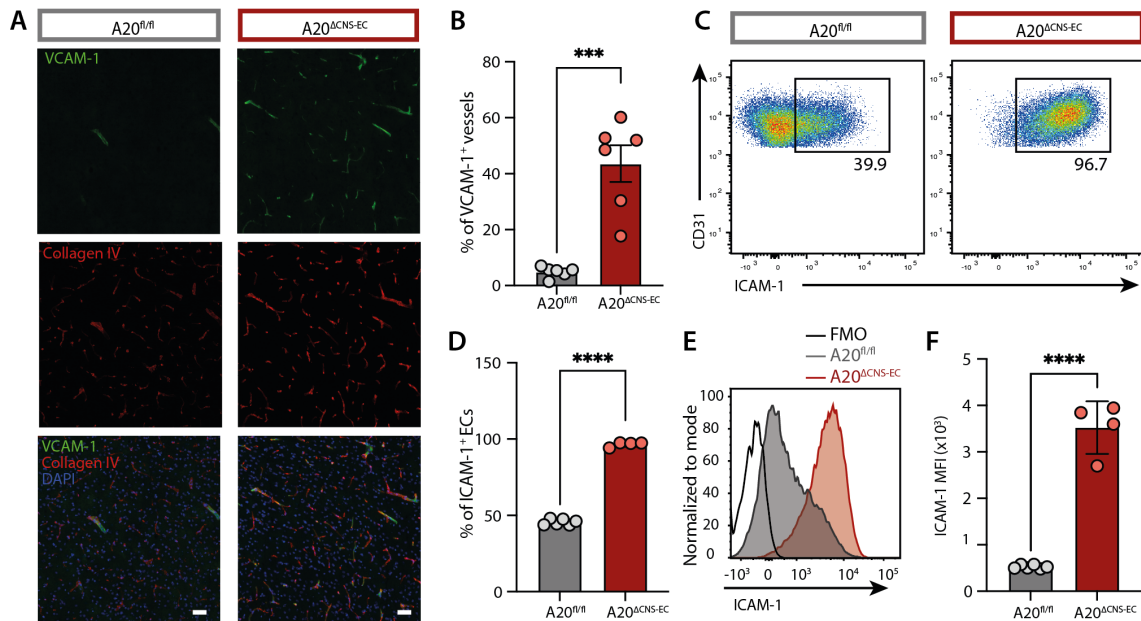
984 **Figure 2: Loss of CNS EC-A20 drives T cell infiltration during EAE and in the steady state**
 985 (A-E) AT-EAE disease was induced in A20^{ΔCNS-EC} mice and A20^{fl/fl} littermate controls. At the peak
 986 of the disease (day post transfer (DPT) 14) SC-infiltrating CD45.1⁺ transferred T cells were
 987 isolated and analyzed by flow cytometry after a MOG recall assay *ex vivo*. (A) Representative
 988 gating strategy for CD40L⁺ CD4⁺ T cells and amongst them frequencies of GM-CSF, IL-17A, IFN-
 989 γ and double-producing cells; pre-gated as single, live, CD45.1⁺ transferred T cells. (B-F)
 990 Quantification of immune cell populations. Data is representative for 2 independent
 991 experiments with n = 6-8 mice per group. (B) Absolute cell numbers of CD45.1⁺ transferred T
 992 cells, (C) CD40L⁺ among transferred T cells, (D) IL-17A⁺, (E) GM-CSF⁺ and (F) IFN-γ⁺ cells
 993 amongst CD40L⁺ cells. (G) Representative immunostainings of CD3⁺ T cells (magenta), CD31⁺
 994 endothelial cells (green) and nuclear staining (DAPI, blue) in the SC at the peak of AT-EAE
 995 (DPT14) of A20^{ΔCNS-EC} and A20^{fl/fl} mice (scale bar = 50 μm). (H-J) Flow cytometric analysis of
 996 CNS-infiltrating cells in the steady state of A20^{ΔCNS-EC} and A20^{fl/fl} mice one week after TAM
 997 treatment. Cells were isolated from pooled SC and brain tissue. (H) Representative gating
 998 strategy for CD45⁺ total immune cells; pre-gated as single, live cells. (I-J) Quantification of
 999 immune cell populations. Data is representative for 3 independent experiments with n = 4-5
 1000 mic per group. (I) Absolute cell numbers of CD45⁺ total infiltrates and amongst them (J)
 1001 number of TCRβ⁺ T cells. Statistical significance was determined by two-tailed unpaired
 1002 Student's t-test. * p<0.05, *** p<0.001.



1003
1004
1005
1006
1007
1008
1009
1010
1011
1012
1013
1014
1015
1016
1017
1018
1019
1020
1021
1022
1023
1024
1025

Figure 3: A20-deficiency in CNS-ECs does not impair BBB integrity

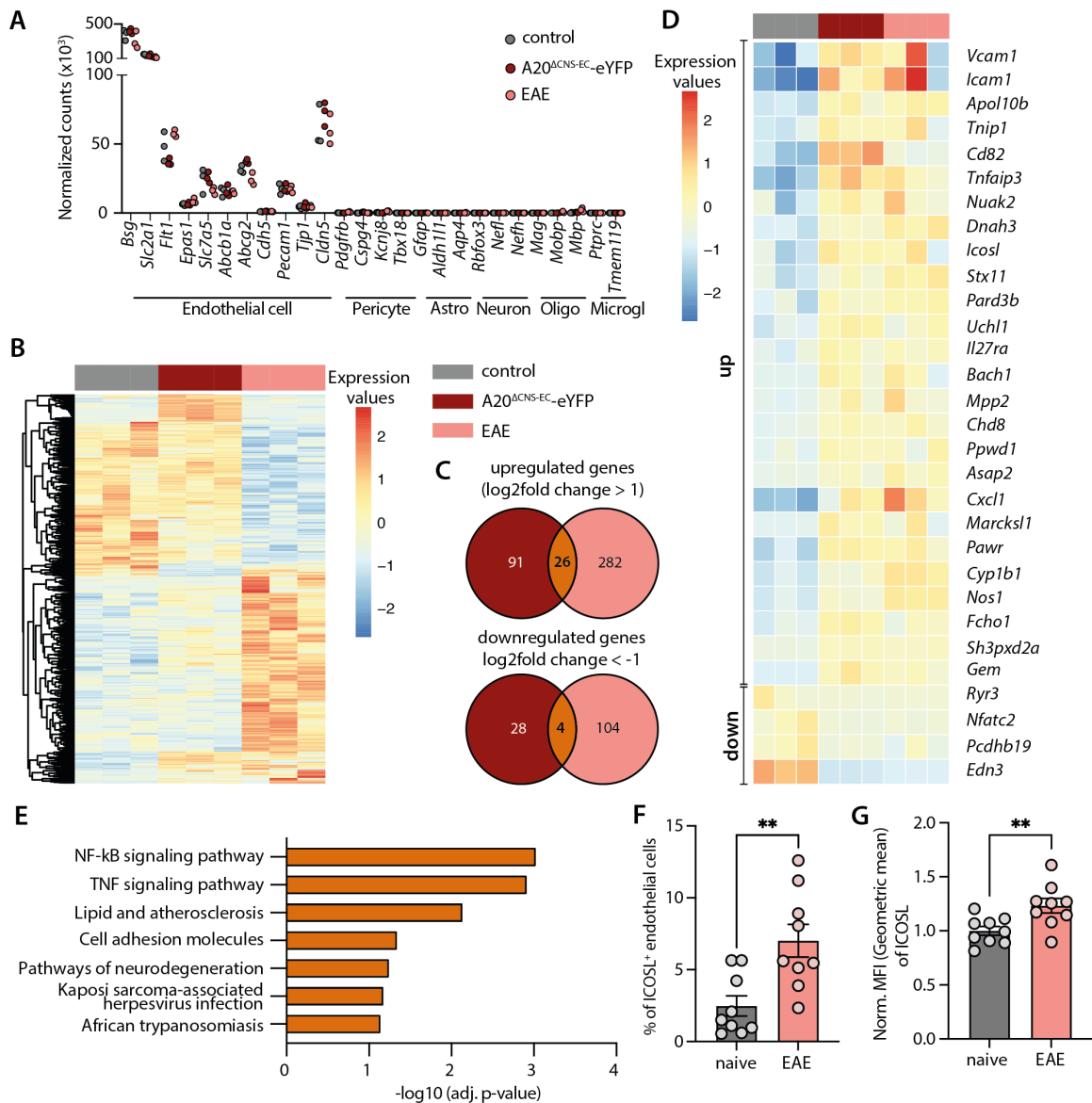
(A-C) Brain sections from A20^{ΔCNS-EC} and A20^{fl/fl} mice were stained for collagen IV (red) and CD31 (green) to determine vessel length and string vessel length. String vessels were identified as capillaries that have lost CD31-positive endothelial cells and only consist of the basement membrane protein collagen IV. Representative microscopic images are shown in (A). Scale bar = 50 μm. (B) Vessel length in mm per mm² and (C) string vessel length [%] normalized to A20^{fl/fl} littermate controls were quantified (n = 5-6 mice per group). (D) Brain weight of A20^{ΔCNS-EC} and A20^{fl/fl} mice (n = 8 mice per group) shown as representative of 2 individual cohorts. (E-F) Brain sections from A20^{ΔCNS-EC} and A20^{fl/fl} mice were stained for occludin (red). Representative microscopic images are shown in (E). Scale bar = 50 μm. (F) Occludin intensity was quantified and is presented relative to A20^{fl/fl} littermate control mice (n = 5-6 mice per group) as representative of 2 individual cohorts. (G-H) A20^{ΔCNS-EC} and A20^{fl/fl} mice were injected with 2 mM 3-5 kDa FITC-dextran in PBS i.p. After 15 minutes, SC and brain were isolated and homogenized in PBS. Fluorescence was measured in the supernatant and raw fluorescence units (RFU) were normalized to tissue weight. PBS injected mice were used as Sham controls; mice at the peak of an active EAE (scores between 1.5 – 3.5) were used as positive controls. Normalized RFUs are shown for SC (G) and brain (H) relative to A20^{fl/fl} controls (SC: n = 5-7; brain: n = 3-5 mice per group). Statistical significance was determined by two-tailed unpaired Student's t-test (B-D, F) or ordinary one-way ANOVA with Tukey's multiple comparisons test (G, H). Ns = not significant, ** p<0.01, **** p<0.0001.



1026
1027
1028
1029
1030
1031
1032
1033
1034
1035
1036
1037
1038
1039
1040
1041

Figure 4: *A20*-deficiency in CNS-ECs drives adhesion molecule expression

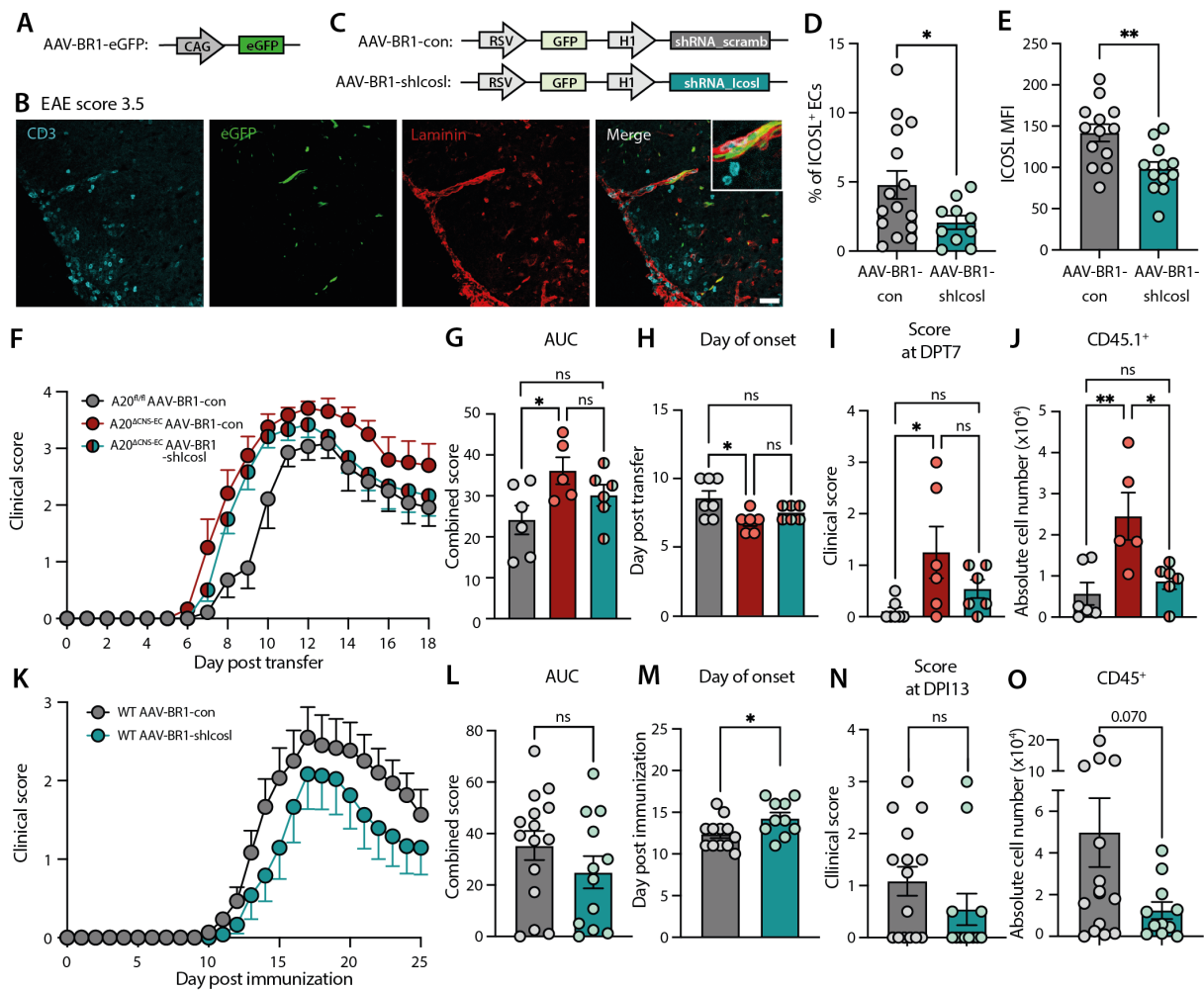
(A-B) Brain sections were stained for VCAM-1 (green) and collagen IV (red) together with a nuclear staining (DAPI, blue). Representative microscopic images are shown in (A). Scale bar = 50 μ m. (B) Frequency of VCAM-1⁺ vessels quantified as percentage of all collagen IV positive vessels (n = 6 mice per group). (C-F) Flow cytometric analysis of ICAM-1 on CNS-ECs isolated from pooled brain and spinal cord tissue from *A20* ^{Δ CNS-EC} and *A20*^{fl/fl} littermate control mice. Data is representative from 3 individual experiments with n = 4-6 mice per group. (C) Representative gating strategy for ICAM-1⁺ CNS-ECs; gate was set based on fluorescence minus one (FMO) control. CNS-ECs were pre-gated as single, live, CD45⁻ CD11b⁻ Ly6C⁺ CD31⁺ cells. (D) Frequency of ICAM-1⁺ ECs quantified as percentage of all CNS-ECs. (E) Histogram of ICAM-1 fluorescence on ECs in *A20* ^{Δ CNS-EC}, *A20*^{fl/fl} mice and FMO control. (F) Mean fluorescence intensity (MFI) presented as geometric mean of ICAM-1 on CNS-ECs. Statistical significance was determined by two-tailed unpaired Student's t-test (B, D, F). *** p<0.001, **** p<0.0001.



1042
1043
1044
1045
1046
1047
1048
1049
1050
1051
1052
1053
1054
1055
1056
1057
1058
1059

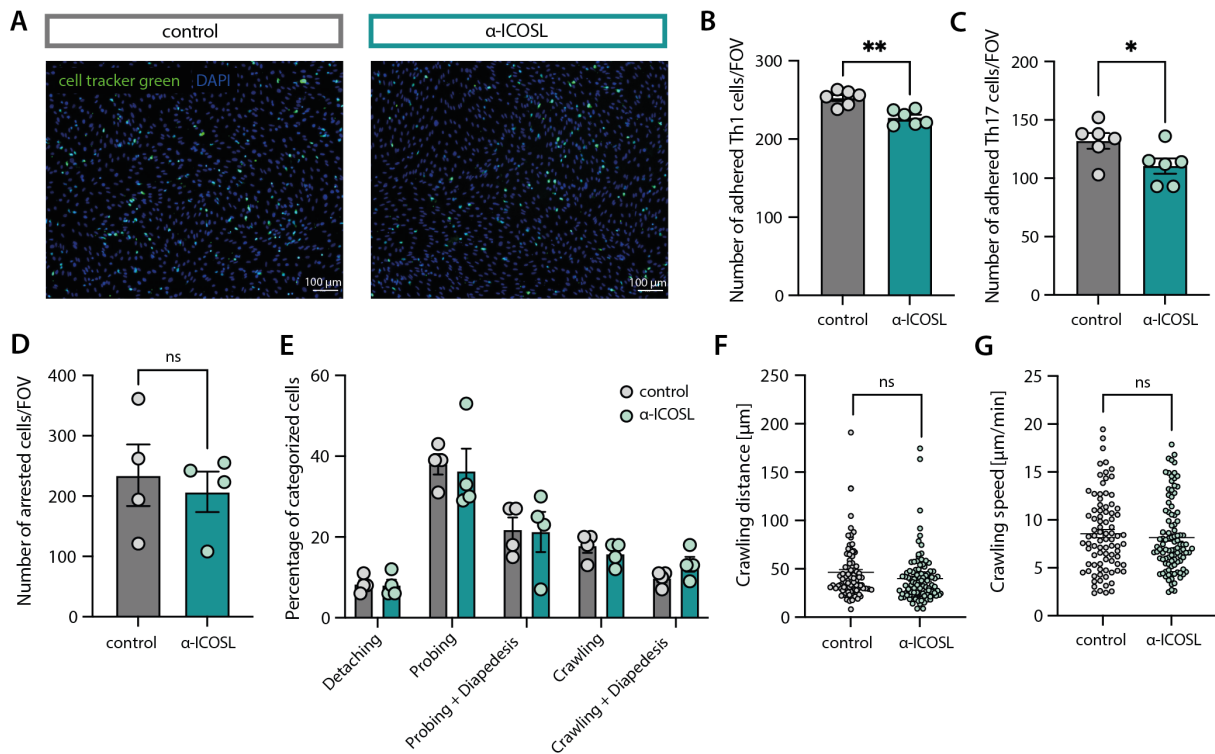
Figure 5: RNA sequencing identifies A20-regulated ICOSL as potential adhesion molecule
(A-E) RNA sequencing of sorted CNS-ECs from SC of naïve A20^{ΔCNS-EC}-eYFP (red), A20^{fl/fl} littermate control mice (referred to as control, grey), and A20^{fl/fl} mice at day 10 after EAE immunization with MOG₃₅₋₅₅/CFA and PTx (referred to as EAE, pink) (n = 3 mice per group). (A) Purity of EC sorting was assessed by plotting normalized counts for marker genes of ECs, pericytes, astrocytes (astro), neurons, oligodendrocytes (oligo) and microglia (microgl). (B) Heatmap showing color-coded standardized z-scores for the expression values of genes differentially regulated in A20^{ΔCNS-EC} or EAE CNS-ECs compared to control. Each column represents an individual mouse. (C) Venn diagrams showing the number of commonly upregulated (log₂fold change > 1) and commonly downregulated (log₂fold change < -1) genes in A20^{ΔCNS-EC}-eYFP and EAE mice compared to control as overlap of the circles. (D) Heatmap showing color-coded standardized z-scores for the expression values of the 30 commonly DE genes. Each column represents an individual mouse. (E) KEGG pathway analysis of the 30 commonly differentially expressed genes shown in (D). (F-G) ECs were isolated from the CNS of wildtype mice at day 10 post immunization with MOG₃₅₋₅₅/CFA and PTx or from naïve mice and stained for flow cytometric analysis of ICOSL. Data is pooled from 3 individual experiments with n = 9 mice per group. (F) Percentage and (G) normalized geometric MFI of ICOSL amongst

1060 all ECs were quantified. Statistical significance was determined by two-tailed unpaired
1061 Student's t-test. ** $p < 0.01$.



1062

1063 **Figure 6: Knockdown of ICOSL on CNS microvascular ECs mildly ameliorates EAE severity**
 1064 (A) Schematic representation of AAV-BR1-eGFP construct. (B) Representative
 1065 immunofluorescence of SC tissue from mice treated with AAV-BR1-eGFP. Tissue was
 1066 harvested at peak of EAE disease and stained for CD3 (cyan) and laminin (red). Endogenous
 1067 eGFP is shown in green. Scale bar = 40 μm . (C) Schematic representation of AAV-BR1
 1068 constructs. (D) Percentage of ICOSL⁺ ECs and (E) MFI (geometric mean) of ICOSL on brain ECs
 1069 in wildtype mice treated with AAV-BR1 constructs and two weeks later immunized with
 1070 MOG/CFA. Analysis was performed at DPI10. Data is pooled from 2 individual experiments
 1071 with n = 10-15 mice per group. (F-J) A20 ^{$\Delta\text{CNS-EC}$} or A20^{fl/fl} controls were treated with AAV-BR1-
 1072 shlcosl or AAV-BR1-con as indicated. One week later, mice were treated with TAM and AT-EAE
 1073 was induced four weeks later (n = 5-7 mice per group). (F) Clinical signs were monitored daily
 1074 and are shown as mean clinical scores \pm SEM. (G) AUC, (H) day of onset and (I) score at DPT7
 1075 analyses from data shown in (F). (J) Flow cytometric analysis of CD4⁺ CD45.1⁺ transferred T
 1076 cells in the SC at DPT18. (K-O) Wildtype mice were injected with AAV-BR1 constructs. Two
 1077 weeks later, mice were immunized with MOG/CFA. (K) Clinical signs were monitored daily and
 1078 are shown as mean clinical scores \pm SEM. Data is pooled from 2 independent experiments
 1079 with n=12-15 mice per group. (L) AUC and (M) day of onset and (N) score at day post
 1080 immunization (DPI) 13 analyses of clinical course shown in (K). (O) Flow cytometric analysis of
 1081 CD45⁺ in the SC at DPI30. Statistical significance was determined by two-tailed unpaired
 1082 Student's t-test (L-O) or ordinary one-way ANOVA with Tukey's multiple comparisons test (G-
 1083 J). ns = not significant, * p < 0.05, ** p < 0.01.



1084
1085
1086
1087
1088
1089
1090
1091
1092
1093
1094
1095
1096
1097
1098
1099
1100
1101
1102
1103
1104
1105

Figure 7: ICOSL regulates T cell adhesion to pMBMECs

(A-C) Static adhesion assay of T cells on pMBMECs. pMBMECs were stimulated with IL-1 β for 72 h and incubated for 30 min with α -ICOSL or control antibody. T cells were labelled with CellTracker™ Green CMFDA dye and added for 30 min to the pMBMECs on a shaking platform. After washing, images were taken and adhering cells were counted. Data is representative for 2 individual experiments with n = 6 per group. (A) Representative microscopic images of 2D2 Th1 cells (green) adhering to the pMBMEC monolayer (nuclear stain blue, DAPI). (B) Quantification of number of adhered 2D2 Th1 cells per field of view (FOV). (C) Quantification of number of adhered 2D2 Th17 cells per FOV. (D-G) Analysis of T cell post-arrest behavior on pMBMECs. Data is pooled from 4 individual experiments. pMBMECs were stimulated with IL-1 β for 72 h and incubated for 30 min with α -ICOSL or control antibody. 2D2 Th1 T cell post-arrest behavior was assessed by live cell imaging under physiological flow. (D) Number of arrested Th1 cells per FOV. (E) Quantification of T cell post-arrest behavior. Each category is shown as fraction of the sum of the categorized cells. (F) Crawling distance of T cells that successfully completed diapedesis on IL-1 β -stimulated isotype or α -ICOSL treated pMBMECs under flow conditions during 20 min observation time shown in μ m. (G) Crawling speed of T cells that successfully completed diapedesis on IL-1 β -stimulated isotype or α -ICOSL treated pMBMECs under flow conditions shown in μ m/min. Data in (F) and (G) is pooled from 4 individual experiments with n = 86-102 tracks analyzed. Data was analyzed using two-tailed unpaired Student's t-test (B-D, F, G) or two-way ANOVA with Šidák's multiple comparison test (E). ns = not significant, * p<0.05, ** p<0.01.